

# 1 Modeling multiple scattering transient of an 2 ultrashort laser pulse by spherical particles

3 GEOFFROY CHAUSSONNET<sup>1</sup>, LOÏC MEES<sup>2</sup>, MILOŠ ŠORMAZ<sup>3</sup>,  
4 PATRICK JENNY<sup>3</sup>, PHILIPPE M. BARDET<sup>1</sup>

5 <sup>1</sup>*George Washington University, 2121 I St NW, Washington, DC 20052, USA*

6 <sup>2</sup>*CNRS, Univ Lyon, Ecole Centrale de Lyon, INSA Lyon, Univ Claude Bernard Lyon 1, LMFA, UMR5509,*  
7 *69134, Ecully, France*

8 <sup>3</sup>*Institute of Fluid Dynamics, ETH Zurich, Sonneggstraße 3, 8092 Zürich, Switzerland*

9 \**gchaussonnet@gwu.edu*

10 **Abstract:** The multiple scattering of an ultrashort laser pulse by a turbid dispersive medium  
11 (namely a cloud of bubbles in water) is investigated by means of Monte Carlo simulations. The  
12 theory of Gouesbet and Gréhan [Part. Part. Syst. Charact. **17** 213-224 (2000)] is used to derive  
13 an energetic model of the scattering transient. It is shown that the spreading and extinction  
14 of the pulse can be decoupled from the transient of scattering, which allows to describe each  
15 phenomenon individually. The transient of scattering is modeled with the Lorenz-Mie Theory  
16 and thus is also valid for a relative refractive index lower than one, contrary to the Debye series  
17 expansion which does not converge close to the critical angle. This is made possible after the  
18 introduction of a new physical object, the Scattering Impulse Response Function (SIRF) which  
19 allows to detect the different modes of scattering transient, in time and direction. The present  
20 approach is more generic, as it enables to simulate clouds of air bubbles in water, which was not  
21 possible previously. Two different approaches are proposed within the Monte Carlo framework.  
22 The first is a pure Monte Carlo approach where the delay due to the scattering is randomly drawn  
23 at each event, while the second is based on the transport of the whole scattering signal. They  
24 are both embedded in the Monte Carlo code Scatter3D [JOSA A **24**, 2206-2219 (2007)]. Both  
25 models produce equivalent trends and are validated against published numerical results. They  
26 are then applied to the multiple scattering of ultra short pulse by a cloud of bubble in water in the  
27 forward direction. The pulse spread due to the propagation in water is computed for a wide range  
28 of traveled distances and pulse durations, and the optimal pulse duration is given to minimize  
29 the pulse spread at a given distance. The main result is that the scattered photons exit the turbid  
30 medium earlier than the ballistic photons and produce a double peak related to the refraction in  
31 the bubble. This demonstrates the possibility to develop new diagnostics to characterize dynamic  
32 bubbly flows.

## 33 1. Introduction

34 The characterization of turbid media appears in a very broad spectrum of applications like  
35 detection of cancerous cells in organic tissues [1], characterization of dense fuel spray in  
36 combustion engines [2], or atmospheric optics [3] to name a few. Such media are by definition  
37 optically thick, which means that when light beams cross turbid media, most of the photons  
38 undergo multiple scattering and very few of them are unaffected. This property makes turbid  
39 media look opaque and conventional optical diagnostics to characterize dynamic media such as  
40 shadowgraphy, laser diffraction or laser Doppler anemometry perform poorly [4]. Solutions were  
41 developed for stationary media based, for example, on periodic polarization modulation [5], or  
42 structured illumination and Fourier filtering [6].

43 The development of ultrashort laser pulse below the picosecond in combination with ultrafast  
44 time gating offers an alternative approach, commonly called ballistic imaging [7]. The method  
45 consists in recording the time of arrival of an ultrafast laser pulse through the medium; it has been  
46 demonstrated in gas flows laden with droplets. In this configuration and with adequate time

47 resolution, the signal reveals a primary peak made of ballistic (no interaction with the suspension)  
48 and snake (only diffraction) photons, followed by a second smoother peak made of scattered  
49 photons. The resolution of these peaks allows to identify the global characteristics of the cloud of  
50 scatterers such as the concentration, the mean diameter, or the width of the size distribution [8].  
51 This technique was experimentally demonstrated by Calba *et al.* [9] with polystyrene particles  
52 immersed in water and by Linne *et al.* [2] in the case of a dense fuel spray.

53 While not studied to date, ballistic imaging could be of interest for dense bubbly flows,  
54 particularly where it is important to record the smallest bubbles. This includes a broad range  
55 of fields, such as environmental flows, nuclear thermal hydraulics, hydraulics, and naval  
56 hydrodynamics. This configuration differs from the ones mentioned above in two aspects. First,  
57 the scatterers (air bubble) have a refractive index lower than that of the propagation medium  
58 (water), which means that refracted photons are faster than ballistic ones [10]. As a result it can  
59 be expected that the peaks of the transmitted light signal might appear in a different order than  
60 those with water droplet in air. Second, due to the significant variations of the water refractive  
61 index in the visible light, dispersion and extinction of the pulse must be accounted for. The  
62 present paper proposes to model the transient multiple scattering of an ultrashort laser pulse  
63 with the LMT to investigate the effect of bubbles characteristics on the output temporal signal.  
64 An important consequence of the relative refractive index lower than one (air bubbles in water)  
65 is the presence of the critical angle of refraction where the Debye series do not converge. In  
66 the pioneering work of Calba *et al.* [8] the scattering transient was described by the Debye  
67 expansion of Lorenz-Mie series, which allows to separate each order of refraction, to facilitate  
68 their identification in time and direction, and finally to greatly simplify the modeling. Since  
69 the Debye series would not converge in the present configuration, it is necessary to modify the  
70 modeling strategy of the scattering transient. In the present work we use the full Lorenz-Mie  
71 Theory (LMT) to have an exact description of the scattering at any angle. In order to differentiate  
72 the peaks of energy in time and direction, we introduce a new physical object, the Scattering  
73 Impulse Response Function (SIRF) which is the virtual response of the scatterer to an infinitely  
74 short pulse. This new approach leads to a better time-separation of the scattering modes, and  
75 enables us to build a more generic model. This is one of the novelties of this work.

76 Multiple scattering in a turbid medium can be modeled by two approaches [3]. The first one starts  
77 from basic differential equations (Maxwell or the wave equation), then incorporates the scattering  
78 and absorption properties of particles. It leads to differential or integral equations describing  
79 statistics such as variances or correlation functions, which account for all phenomena such as  
80 multiple scattering, diffraction, and interferences. This approach is mathematically rigorous,  
81 but the resolution of the equations is in practice computationally prohibitive. Alternatively, the  
82 radiative transfer theory is based on the transport of energy through a medium containing particles.  
83 It is described by the Radiative Transfer Equation (RTE) which is equivalent to Boltzmann's  
84 equation from the kinetic theory of gases. It neglects self interactions of the electromagnetic  
85 field during propagation, such as interference, enabling the superposition principle for intensities  
86 and powers. The electromagnetic effects due to the particles such as diffraction and interference  
87 at the particle scale are accounted by an appropriate modeling of the scattering, such as the  
88 LMT. This approach is thus phenomenological and allows to solve various practical problems  
89 such as atmospheric and underwater visibility, marine biology, and photographic emulsions [3].  
90 It was shown recently that when averaged over a sufficiently long period of time, Maxwell's  
91 electromagnetic theory for multiple wave scattering in discrete random media can be related to  
92 the radiative transport theory [11, 12].

93 The radiative transfer theory was selected for the present study. To accurately predict the  
94 propagation of an ultrashort pulse through a turbid medium seeded with large scatterers (1 -  
95 100  $\mu\text{m}$ ), the transient of scattering must be accounted for [13], which is the case here. Therefore  
96 we need to incorporate the transient of the LMT into the scattering model of the RTE. To do this

97 we use the theory of Gouesbet and Gréhan [14] that describes far field temporal single scattering  
 98 of an electromagnetic (EM) pulse. The structure of this study is as follows. In Section 2 we  
 99 derive the multiple scattering transient in a dispersive medium based on the theory of Gouesbet  
 100 and Gréhan [14]. The results are then adapted to the radiative transport theory and the Monte  
 101 Carlo method is presented in Section 3. The spread of an ultrashort pulse in water is discussed  
 102 in Section 4. Numerical aspects of the model are investigated in Section 5, and the present  
 103 approach is validated in the case of single scattering in Section 6. Finally, the transient of multiple  
 104 scattering is compared to other numerical simulations from the literature in Section 7 followed  
 105 by more realistic simulations in Section 8.

## 106 2. Transient scattering due to an electromagnetic pulse

107 This section details the mathematical aspect of the transient of multiple scattering in a dispersive  
 108 medium and how it can be decomposed into convolution products. First the spreading of a pulse  
 109 is presented, followed by single scattering and multiple scattering.

### 110 2.1. Pulse spreading in a dispersive medium

111 Let  $\psi$  be the incident electric (E) or magnetic (H) field for a pulsed plane wave in a dispersive  
 112 medium. We assume that a laser located at  $z = -L$  (Fig. 1) produces a Gaussian pulse whose peak  
 113 is at  $z = -L$  at the time  $t = -T \equiv -L/v_g$  where  $v_g$  is the group velocity defined by  $v_g = \partial\omega/\partial k$   
 114 at the carrier frequency  $\omega_0$ .

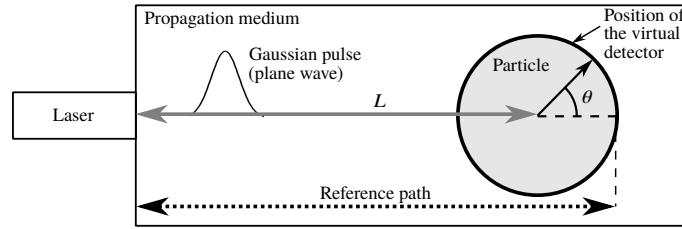


Fig. 1. Sketch of the modeled configuration.

115 The temporal envelop  $g$  of the pulse at the laser location and its Fourier Transform (FT)  $G$   
 116 read:

$$g(t, z = -L) = \exp \left[ - \left( \frac{t + T}{\gamma} \right)^2 \right] \quad \text{and} \quad G(\omega) = \frac{\gamma}{\sqrt{2}} e^{-(\gamma\omega/2)^2} \quad (1)$$

117 where  $\gamma$  is a time constant related to the Full Width at Half Maximum (FWHM)  $\Delta t$  for a Gaussian  
 118 envelope:

$$\gamma = \frac{\Delta t}{2\sqrt{\log(2)}} \quad (2)$$

119 We assume that the center of a particle is located at  $z = 0$ . With the definition of  $L$ , the peak of  
 120 the pulse would reach  $z = 0$  at  $t = 0$  if no particle were here. The incident plane wave at the  
 121 particle location can be expressed in the time domain by the Inverse Fourier Transform (IFT):

$$\psi(t, z) = \frac{\psi_0}{\sqrt{2\pi}} \int_0^{+\infty} e^{i(\omega t - kz)} G(\omega - \omega_0) e^{i(\omega T - kL)} d\omega \quad (3)$$

122 where  $k = \omega/c$  is the wave vector and  $\psi_0$  is the amplitude of the incident wave. The argument of  
 123 the second complex exponential in Eq. 3 can be written as  $iL(\omega/v_g - k)$  which represents of the

124 pulse spreading over the distance  $L$  between the laser source and the particle. It is convenient to  
 125 gather the pulse and its propagation to express the FT of the chirped pulse as:

$$G'(\omega - \omega_0, L) = G(\omega - \omega_0) e^{iL(\omega/v_g - k)} \quad (4)$$

126 Note that in a dispersive and absorbing medium the wave vector  $k$  is complex and has a non-linear  
 127 dependency on the frequency  $\omega$ . The envelop  $g'$  of the chirped pulse is the slowly varying signal  
 128 from Eq. 3. Its expression is given by taking out the carrier oscillations  $(\omega_0, \Re(k_0))$  from Eq. 3.  
 129 In the following, we will consider the envelop  $g'$  of the chirped pulse after an optical path of  
 130 length  $L$  in the dispersive medium:

$$g'(t, L) = \frac{1}{\sqrt{2\pi}} \int_0^{+\infty} e^{i[(\omega - \omega_0)(t - L/v_g) - (k - \Re(k_0))L]} G(\omega - \omega_0) d\omega \quad (5)$$

131 where  $\Re(k_0)$  is the real part of  $k_0$ .

## 132 2.2. Transient of single scattering

133 According to the theory of Gouesbet and Grehan [14], the transient of the scattering is expressed  
 134 in the frequency domain and transformed back in the time domain by an IFT:

$$\psi^s(t, \theta, L) = \mathcal{F}^{-1}[G'(\omega - \omega_0, L) \psi^{cw}(\omega, \theta)] \quad (6)$$

135 where  $\mathcal{F}^{-1}$  represent the IFT and the superscript  $cw$  stands for a continuous wave. The term  
 136  $\psi^{cw}(\omega, \theta)$  represents the scattered field in the polar direction  $\theta$  for a continuous monochromatic  
 137 illumination at the frequency  $\omega$ , and it is determined from the LMT. Within the LMT,  $\psi^{cw}$   
 138 depends only on the size parameter and the relative refractive index, respectively:

$$x \equiv \pi d_s n_{pm} / \lambda_0 = r_s n_{pm} \omega / c_0 \quad \text{and} \quad m \equiv n_s / n_{pm} \quad (7)$$

139 where  $d_s$  and  $r_s$  are the scatterer diameter and radius, and  $\lambda$  the wavelength in vacuum of the  
 140 incident wave. The terms  $n_{pm}$  and  $n_s$  are the complex refractive indices of the propagation  
 141 medium and the scatterer, respectively. The size parameter  $x$  depends on  $\omega$ , and so does  $m$  for a  
 142 dispersive medium, which means that  $\psi^{cw}$  implicitly depends on  $\omega$ . In the following we drop the  
 143 dependency of  $\psi^{cw}$  on  $x$  and  $m$  for the sake of clarity, but we keep the implicit dependency on  $\omega$ .  
 144 The term  $\psi^s(t, \theta, L)$  in Eq. 6 is the far field EM wave scattered by the particle in the polar  
 145 direction  $\theta$  at time  $t$ . The parameter  $L$  mentions that before impacting the scatterer, the pulse  
 146 traveled a distance  $L$  in the dispersive medium. In the present expression we suppose that the  
 147 virtual detector is located on the scatterer surface so that the pulse spreading after the scattering  
 148 is not considered. In [15], the time  $t$  is chosen according to a time of reference given by the path  
 149 traveling in propagation medium only from the laser to the location of the center of the particle,  
 150 then to a virtual detector located in the far-field. However we define here the reference time as  
 151 the propagation time from the laser source to the further boundary of the scatterer (Fig. 1). This  
 152 can be approximately regarded as if a virtual detector were located at the surface of the particle  
 153 and were recording the far-field scattering signal for all directions  $\theta$  (Fig. 1). Hence,  $t = 0$  when  
 154 the maximum of the pulse reaches the position of the scatterer further boundary. Also, contrary  
 155 to the study by [15], we choose the sign of the time so that it increases as it elapses. Thus we  
 156 define  $t'$  as:

$$t' = \frac{d_s}{v_g} - t \quad (8)$$

157 In this case,  $t' < 0$  represents an optical path shorter than the reference path. In the following,  
 158 we drop the prime symbols ( $'$ ) from  $t'$  for the sake of clarity and we write  $t \equiv t'$ . Finally, the  
 159 scattered field is given by:

$$\psi^s(t, \theta, L) = \frac{1}{\sqrt{2\pi}} \int_{\omega_{\min}}^{\omega_{\max}} G(\omega - \omega_0) e^{i(\omega T - kL)} \psi^{cw}(\omega, \theta) e^{i\omega t} d\omega \quad (9)$$

160 where  $\omega_{\min}$  and  $\omega_{\max}$  are the bounds where  $G(\omega)$  is significantly larger than 0, and  $T = L/v_g$ .

161

162 Note that when  $\omega$  is negative we use the relation  $\psi^{cw}(\omega) = \psi^{cw*}(-\omega)$ , where the super-  
 163 script  $*$  stands for the complex conjugate. In the following, the scattered intensity is expressed as  
 164  $I_i = |\psi^s(t)|^2$  where the index  $i$  can take the symbols 1 and 2 for the electric field in the incident  
 165 and in the perpendicular to the planes, respectively. When no index is mentioned, the EM wave  
 166 is assumed non-polarized and  $I = (I_1 + I_2)/2$ .

167 Now we inspect each terms of Eq. 9 in the frequency domain, where it is a product of three terms:

$$\mathcal{F}[\psi^s](\omega, \theta, L) = \underbrace{G(\omega - \omega_0)}_{\text{Pulse}} \underbrace{e^{i(\omega T - kL)}}_{\text{Dispersion}} \underbrace{\psi^{cw}(\omega, \theta)}_{\text{Scattering}} \quad (10)$$

168 The terms of the RHS are, in order of appearance, (i) the FT of the pulse as it exits the laser, (ii)  
 169 the FT of the dispersion operator, which describes the spreading of the pulse from the laser to the  
 170 particle, and (iii) the scattering operator. We can make several remarks on Eq. 10. First, when  
 171 the medium is non-dispersive, the dispersion operator is reduced to  $\mathcal{D}(\omega) = 1$ . Second, contrary  
 172 to the pulse and the dispersion terms, the scattering term  $\psi^{cw}$  is not the result of a FT, but was  
 173 derived by Mie [16] for a monochromatic incident wave. Hence, it can be expressed directly in  
 174 the frequency domain.

175 Formally writing the RHS of Eq. 10 as FT and using the convolution theorem, one can see the  
 176 transient of the scattering in a dispersive medium as the time convolution product of three terms:

$$\psi^s(t, \theta, L) = g(t, -L) * d(t, L) * \phi(t, \theta) \quad (11)$$

177 where  $d(t, L)$  is the time signal of the dispersion operator. The optical path is  $-L$  for the pulse  
 178 term because the origin of the coordinates system is the scatterer center. The two first terms of  
 179 the RHS can be merged in  $g'$  to represent the time signal of the incident chirped pulse:

$$\psi^s(t, \theta, L) = g'(t, L) * \phi(t, \theta) \quad (12)$$

180 The last factor of the RHS of Eqs. 11 and 12 is the impulse response function of the scatterer. It  
 181 corresponds to the scatterer response to an infinitely short light pulse, *i.e.* a Dirac delta function.  
 182 Since it plays a particular role in the following we drop the letter  $\psi$  and label it  $\phi$  instead. It is  
 183 expressed as:

$$\phi(t, \theta) = \mathcal{F}^{-1}[\psi^{cw}(\omega, \theta)] = \frac{1}{\sqrt{2\pi}} \int_{-\infty}^{\infty} \psi^{cw}(\omega, \theta) e^{i\omega t} d\omega \quad (13)$$

184 In the following  $\phi(t, \theta)$  is referred to as the Scattering Impulse Response Function (SIRF). Note  
 185 that the original solution of the LMT derived by Mie [16] can be seen from the same viewpoint.  
 186 Indeed, the temporal response  $s_{\omega_0}(t)$  of a scatterer illuminated by a monochromatic light source  
 187 of frequency  $\omega_0$  is the convolution of the SIRF by a pure sine function, which in the frequency  
 188 domain is equal to the Dirac delta function. Hence:

$$s_{\omega_0}(t, \theta) = \frac{1}{\sqrt{2\pi}} \int_{-\infty}^{\infty} \delta(\omega - \omega_0) \psi^{cw}(\omega, \theta) e^{i\omega t} d\omega = \psi^{cw}(\omega_0, \theta) e^{i\omega_0 t} \quad (14)$$

189 Numerically speaking, it may not be possible to calculate the SIRF exactly. When  $\omega \rightarrow \infty$ , the  
 190 parameter size  $x$  also tends to infinity, which forbids any application of the LMT. The use of  
 191 geometrical optics for large  $x$  could be used, but not when the relative refractive index  $m < 1$   
 192 (*e.g.* air bubble in water) where the geometrical optics approximation cannot be satisfied near  
 193 the critical angle [17]. To circumvent the exact computation of the SIRF, we smooth the delta

194 function to allow numerical integration of Eq. 13. It is referred to as the SSIRF (Smoothed SIRF)  
 195 method in the following. The SSIRF  $\phi_S$  is the response of the scatterer not to a Dirac delta  
 196 function, but to a very short, finite pulse. Considering a virtual ultra short pulse as a Gaussian  
 197 with a FWHM  $\Delta t_v$  of a few electromagnetic wave cycles  $2\pi/\omega_0$ :

$$\phi_S(t, \theta) = \frac{\gamma}{2\sqrt{\pi}} \int_{\omega_{\min}}^{\omega_{\max}} e^{-[\gamma(\omega-\omega_0)/2]^2} \psi^{cw}(\omega, \theta) e^{i\omega t} d\omega \quad (15)$$

198 with  $\gamma$  expressed by Eq. 2 with  $\Delta t_v$ . In this case, the smoothed impulse response is a signal  
 199 whose peak thickness is at least  $\Delta t_v$ , which decreases the temporal exactness of the SIRF. This  
 200 is the inherent counterpart of smoothing the Dirac delta function. There are limitations on the  
 201 minimal  $\Delta t_v$ . First, the pulse cannot be shorter than one cycle of the EM wave, otherwise the  
 202 mean value of the pulse would be larger than zero, meaning that the Fourier spectrum admits a  
 203 DC component. In this case it would be necessary to propagate with the EM wave a transverse  
 204 DC potential, constant in space, which is impossible. This is known as the "zero-area" rule of a  
 205 propagating pulse [18]. Second, as for the SIRF, large frequencies lead to a large size parameter  
 206 whose calculation is computationally expensive. Third, in the case of dispersive media (both the  
 207 propagation medium or the scatterer medium), it is necessary to know the refractive index over  
 208 the whole variation range of the frequency.

209 Despite these limitations, the smoothed impulse response  $\phi_S(t, \theta)$  of the temporal scattering  
 210 phase function allows to recover the physics of scattering, as validated later. Also, as long as the  
 211 zero-area rule is respected, the SSIRF is a time signal that corresponds to a realistic physical  
 212 phenomenon, and therefore it can be used as standalone model for the scatterer response.

213 For illustration, the SSIRF is shown in Fig. 2 (left) as a map in the  $(\theta, t)$  space. The time  
 214 signal corresponding to different angles is given on the right of the figure. The vertical lines  
 215 superimposed on the map mark the direction where the time signals are plotted. Note that the  
 216 time signal of the stripes at  $t > 0.8$  ps are not visible for angles  $\geq 45^\circ$  because their relative  
 217 intensity  $I/I_{max}$  decreases below the limits of the figure ( $10^{-12}$ ).

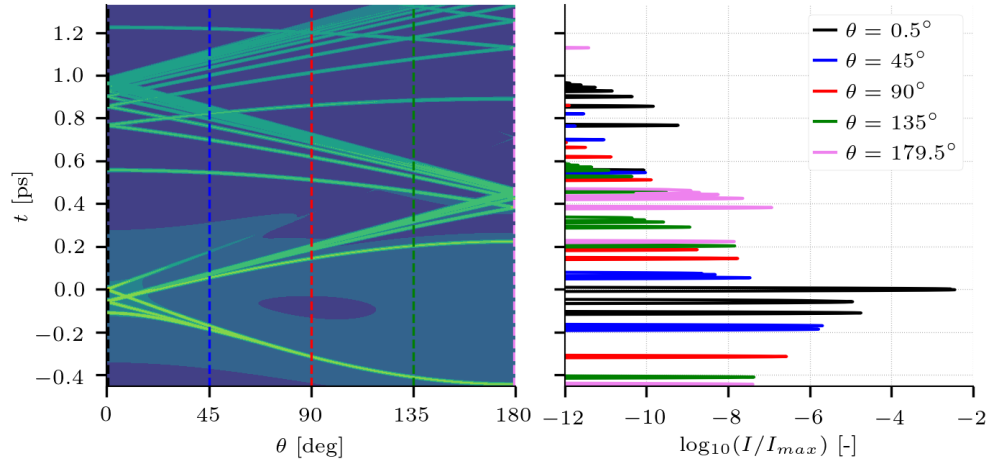


Fig. 2. Left:  $(\theta, t)$ -map of the SSIRF for a bubble of  $100 \mu\text{m}$  ( $x \approx 500$ ) and  $\Delta t_v = 4\pi/\omega_0$ .  
 Right: corresponding time signal at different angles.

### 218 2.3. Transient of multiple scattering

219 Decomposing the scatterer response into different terms (Eqs. 10-12) enables to decouple the  
 220 sources that contribute to the final temporal signal. This is particularly useful when modeling

221 multiple scattering. The scattering of an ultrashort pulse by  $N$  scatterers in a dispersive media  
 222 can be formally expressed in the temporal domain by using Eq. 11:

$$\psi^s(t, \theta) = g(t, -L_0) * \underbrace{d(t, L_0) * \phi(t, \theta_0)}_{1^{\text{st}} \text{ event}} * \underbrace{d(t, L_1) * \phi(t, \theta_1)}_{2^{\text{nd}} \text{ event}} * \dots * \underbrace{d(t, L_{N-1}) * \phi(t, \theta_{N-1})}_{N^{\text{th}} \text{ event}} \quad (16)$$

223 Using the convolution theorem one can express Eq. 16 in the frequency domain:

$$\begin{aligned} \mathcal{F}[\psi^s](\omega, \theta) &= G(\omega - \omega_0) \times e^{i(\omega T_0 - k L_0)} \psi^{cw}(\omega, \theta_0) \\ &\quad \times e^{i(\omega T_1 - k L_1)} \psi^{cw}(\omega, \theta_1) \\ &\quad \dots \\ &\quad \times e^{i(\omega T_{N-1} - k L_{N-1})} \psi^{cw}(\omega, \theta_{N-1}) \end{aligned} \quad (17)$$

224 where  $T_i$  and  $L_i$  are respectively the propagation time and the optical path length between events  
 225  $i - 1$  and  $i$ , for  $i > 0$ ; and  $\theta_i$  is the scattering angle for the event  $i$ . The angle  $\theta$  in the LHS is the  
 226 summation of all scattering angles  $\theta = \sum \theta_i$ . By gathering the terms, we obtain:

$$\mathcal{F}[\psi^s](\omega, \theta, L) = G(\omega - \omega_0) e^{i(\omega T_t - k L_t)} \prod_i \psi^{cw}(\omega, \theta_i) \quad (18)$$

227 where  $(T_t, L_t) = (\sum T_i, \sum L_i)$ . Equation 18, as Eq. 10, can be regarded as a product of three terms  
 228 corresponding to (i) the non-chirped pulse from the laser, (ii) the dispersion term corresponding  
 229 to the whole optical path from the laser to the last scatterer and (iii) the scattering term repeated  
 230  $N$  times for different angles. When inverted into the time domain, Eq. 18 is the time signal on a  
 231 virtual detector located on the last scatterer surface and recording the far field EM wave in the  
 232 polar  $\theta$  direction at time  $t$ . It yields:

$$\psi^s(t, \theta, L_t) = g(t, L_t) * d(t, L_t) * \bigotimes_i \phi(t, \theta_i) \quad (19)$$

233 where the large dyadic symbol  $\otimes$  represents multiple convolutions. Equation 19 can be written  
 234 down:

$$\psi^s(t, \theta, L_t) = g'(t, L_t) * \bigotimes_i \phi(t, \theta_i) \quad (20)$$

235 where the first term represents the pulse spreading due to dispersion and the second term  
 236 represents scattering. Note that Eqs. 19 and 20 refer to only one photon and one trajectory.  
 237 Indeed, the total optical path length  $L_t$  inside the dispersive medium depends on the series of  
 238 scattering angles  $(\theta_0 \dots \theta_{N-1})$  which define a possible way to reach the  $N^{\text{th}}$  scatterer from the  
 239 laser source. The same comments goes to the time signal  $\bigotimes_i \phi(t, \theta_i)$ . Hence Eqs. 19 and 20  
 240 must be integrated over all the possible scenarii represented by  $(\theta_0 \dots \theta_{N-1})$ . This is discussed in  
 241 the next section. Also, note that  $L_t$  is the total path length of the photon inside the dispersive  
 242 medium and does not include the path length inside the scatterer.

243 In the case of particles of different diameters Eqs. 18 and 20 yield:

$$\mathcal{F}[\psi^s](\omega, \theta, L_t) = G(\omega - \omega_0) e^{i(\omega T_t - k L_t)} \prod_i \psi_{d_i}^{cw}(\omega, \theta_i) \quad (21a)$$

$$\psi^s(t, \theta, L_t) = g'(t, L_t) * \bigotimes_i \phi_{d_i}(t, \theta_i) \quad (21b)$$

244 where the subscript  $d_i$  indicates a scattering event by a particle of diameter  $d_i$ .

245 **3. Temporal Monte Carlo techniques**

246 **3.1. Solving the Radiative Transfer Equation**

247 The Monte Carlo (MC) technique is a stochastic method to solve the deterministic RTE given by:

$$\frac{1}{c} \frac{\partial}{\partial t} I(\mathbf{z}, \boldsymbol{\Omega}, t) + \frac{\partial}{\partial z} I(\mathbf{z}, \boldsymbol{\Omega}, t) = -(k + s)I(\mathbf{z}, \boldsymbol{\Omega}, t) + s \int_{4\pi} I(\mathbf{z}, \boldsymbol{\Omega}, t) f(\boldsymbol{\Omega}, \boldsymbol{\Omega}', t) d\boldsymbol{\Omega}' \quad (22)$$

248 where  $I(\mathbf{z}, \boldsymbol{\Omega}, t)$  is the intensity at location  $\mathbf{z}$  propagating in the direction  $\boldsymbol{\Omega}$  at time  $t$ . The terms  
 249  $k$  and  $s$  are the absorption and scattering coefficients, respectively. The second term on the  
 250 RHS represents the scattering in all directions where  $d\boldsymbol{\Omega}'$  is the elementary solid angle about  
 251 the direction  $\boldsymbol{\Omega}'$  and  $f(\boldsymbol{\Omega}, \boldsymbol{\Omega}', t)$  is the time-dependent phase function. The LHS is the total  
 252 derivative in an Eulerian frame and can be written in the Lagrangian frame as  $dI(\mathbf{z}, \boldsymbol{\Omega}, t)/(c dt)$ .  
 253 Equation 22 is based on the assumption that interferences are negligible. This is justified by two  
 254 sets of assumptions. First, the wavelength is negligible versus the dimension of the domain and  
 255 the mean inter scatterer distance. Second, in our configuration the occurrence of interference is  
 256 further diminished because the scatterers have a large parameter size ( $x > 100$ ), thus promoting  
 257 forward scattering, and (ii) the laser pulse is ultrashort, thus the wavefront is localized in space  
 258 and time. These two reasons decrease the probability that different optical paths of the coherent  
 259 wave front will cross each other and interfere.

260  
 261 When solving Eq. 22 with the MC method, each ray of light is represented by an energy quanta  
 262 (referred to as “photon” for convenience) traveling in the turbid medium and carrying the same  
 263 quantity of elementary energy. When a photon undergoes a scattering event, the scattering angle  
 264 is randomly drawn according to a given Probability Density Function (PDF), which corresponds  
 265 to the phase function. This method can be regarded as converting the anisotropic redistribution  
 266 of energy in different directions after the scattering to a probability to have a photon with the  
 267 same directions. As a particle method, the MC method is very versatile and the whole history  
 268 of the particle can be accounted for such as the trajectory, the number of scattering event, etc,  
 269 which allows a deep insight in the scattering phenomenon. This approach was used to model  
 270 transient of multiple scattering based on the photon time of flight only [2, 19], or with accounting  
 271 the transient inside large scatterers [8, 9, 13, 20].

272 **3.2. Energy transport approximation**

273 To make the link between the radiative transport theory that describes power and intensity, and  
 274 the transient of scattering that describes amplitudes of electromagnetic waves, it is necessary to  
 275 express the power of the scattering transient. Therefore, we consider the signal of the intensity  
 276  $I(t, \theta)$  recorded by a time detector capable of resolving different directions. It is found by taking  
 277 the squared modulus of Eq. 21b:

$$I(t, \theta, L_t) = |\psi^s(t, \theta)|^2 = \left| g'(t, L_t) * \bigotimes_i \phi_{d_i}(t, \theta_i) \right|^2 \quad (23)$$

278 Although exact, Eq. 23 is not practical to transport particles of energy in the turbid media because  
 279 the convolutions are applied to the EM wave amplitudes. Therefore, we assume that we can  
 280 distribute the modulus ( $|\cdot|^2$ ) inside the convolutions, *i.e.* that the energy of the photon follows  
 281 the same time distribution as its complex amplitude:

$$I(t, \theta, L_t) \approx |g'(t, L_t)|^2 * \bigotimes_i |\phi_{d_i}(t, \theta_i)|^2 \quad (24)$$

282 Again, this approximation is justified by the fact that interference can be neglected. Equation 24  
 283 is rewritten in terms of intensity:

$$I(t, \theta, L_t) \approx I_p(t, L_t) * I_{\phi, d_0}(t, \theta_0) * I_{\phi, d_1}(t, \theta_1) * \dots * I_{\phi, d_{N-1}}(t, \theta_{N-1}) \quad (25)$$

284 where  $I_p(t, L_t) = |g'(t, L_t)|^2$  is the intensity of the incident pulse after a propagation on distance  
 285  $L_t$ . The sequential convolution in this equation allows us to model the scattered intensity collected  
 286 by a detector with a PDF, as shown in the next section.

### 287 3.3. Two modeling approaches

288 In the rest of this study we will compare two different methods to compute the scattering delay  
 289 in single or multiple scatterings. Both methods are formulated with the energy approximation  
 290 although they would be also valid when transporting the amplitude (and therefore considering  
 291 the polarization). The first method is a pure Monte Carlo method, and referred to as Method 1.  
 292 For each scattering event, the delay is randomly drawn according to a given multivariate PDF  
 293 depending on time and direction. In case of multiple scattering, the total delay due to scattering  
 294 is the sum of the delay of each event. Let us consider  $I(t, \theta)$  in Eq. 25 as the time signal on a  
 295 detector able to separate the different incident angles.  $I(t, \theta)$  can be regarded as a multivariate  
 296 PDF to determine  $(t, \theta)$ . Since  $I(t, \theta)$  is expressed as multiple products of convolution, we can  
 297 benefit from the fact that the random variable described by a convolution of two PDFs is equal to  
 298 the sum of the random variables described by the two PDFs. Let us define the random variable  
 299  $T_{g'}$  as the "in-time" position of the photon in the pulse, and associate it to the univariate PDF  
 300 given by  $I_p(t, L)$ . In the same manner we define the random variables  $(T_i, \Theta_i)$  as the time and  
 301 direction of the scattered photon after the  $i^{\text{th}}$  event and we associate them to the multivariate PDF  
 302  $I_{\phi, d_i}(t, \theta)$ . Therefore, the random variables  $T_{\text{detector}}$  and  $\Theta_{\text{detector}}$ , respectively defined as the time  
 303 and direction of the photon impacting the detector are written:

$$\Theta_{\text{detector}} = \Theta_0 + \Theta_1 + \dots + \Theta_{N-1} \quad (26a)$$

$$T_{\text{detector}} = T_{g'|L} + T_0|_{\Theta_0} + T_1|_{\Theta_1} + \dots + T_{N-1}|_{\Theta_{N-1}} \quad (26b)$$

304 where  $N$  is the number of scattering events. Equation 26b shows conditional probability with  
 305  $T_{g'|L}$  being the random variable of the pulse delay given a optical path length  $L$  and  $T_i|_{\Theta_i}$  being  
 306 the univariate random variable on scattering time in the polar direction  $\Theta_i$ . We use the SSIRF as  
 307 the multivariate PDF, hence in Eq. 25  $I_{\phi, d_i}(t, \theta) = |\phi_S(t, \theta)|^2$  with  $\phi_S(t, \theta)$  expressed by Eq. 15  
 308 for a given diameter  $d_i$ . Note that this is physically consistent because the SSIRF is computed  
 309 over at least one cycle of the electromagnetic wave and hence it respects the zero area rule. This  
 310 means that the PDF depicts a physical phenomenon and a random generator based on this PDF  
 311 renders a physically consistent stochastic signal.

312 The algorithm of Method 1 is sequentially described as follows and illustrated in Fig. 3. A  
 313 numerical photon is shot at the left inlet boundary of the slab. At each scattering event, first the  
 314 polar angle of scattering is randomly drawn according to the marginal univariate Cumulative  
 315 Density Function (CDF)  $F(\theta)$  defined between 0 and  $\pi$  by:

$$F(\theta) = \int_0^\theta f(u) \sin(u) du \quad \text{with} \quad f(u) = \int_{t_{\min}}^{t_{\max}} I_\phi(t, u) dt \quad (27)$$

316 In other words  $F(\theta)$  represents the polar distribution of the energy integrated in time when a  
 317 short pulse is scattered by a spherical particle. It is different from the steady state scattering phase  
 318 function because it filters out potential interferences between different refraction modes [10, 15].  
 319 Since we consider only the energy, we neglect the polarization information and hence the  
 320 azimuthal scattering angle  $\Phi_i$  is equally distributed between 0 and  $2\pi$ . Once  $\Theta_i$  is selected,  
 321 we randomly draw the scattering delay  $T_i|_{\Theta_i}$  according to the CDF  $H(t, \Theta_i) = \int_{t_{\min}}^t I(t', \Theta_i) dt'$ ,

322 which is added to the total scattering time later detected. After this ( $i^{\text{th}}$ ) event the photon  
 323 is deflected in the direction given by  $(\Theta_i, \Phi_i)$ . As detailed below, the distance between two  
 324 scattering events, and the scatterer diameter are randomly drawn according to an exponential  
 325 distribution, and a prescribed droplet size distribution, respectively. When the photon exits the  
 326 slab and reaches the detector, the total optical path is converted into the time necessary to travel  
 327 this distance. This is the time of flight of the photon. In case of the photon flying through a  
 328 dispersive medium, the pulse spread is taken into account by considering the optical path inside  
 329 the dispersive medium. The “in space” spread is converted into “in time” spread, which can be  
 330 considered at first order as increasing the variance of the initial Gaussian pulse, provided that  
 331 the pulse has still a Gaussian profile. This pulse is then expressed in terms of CDF by the error  
 332 function of zero mean and  $\sigma$  standard deviation as  $I_p(T_g', L) \propto \text{erf}(T_g', 0, \sigma(L))$ . Also note that  
 $L$  in  $I_p(T_g', L)$  is an input parameter of the CDF. From an algorithmic point of view, this method

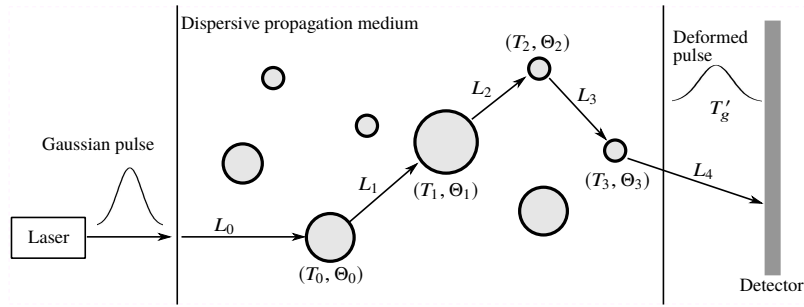


Fig. 3. 2D Sketch of the pure Monte Carlo approach.

333 is easy to implement but requires to load the map  $I(t, \theta)$  for each diameter of the particles. Also,  
 334 it requires a very large amount of photons to converge, as seen later.  
 335

336  
 337 The second method was originally proposed by Calba *et al.* [8]. After a scattering event,  
 338 the numerical photon does not only transport one single scattering delay, but the whole time  
 339 signal such as  $I_{\phi, d_0}(t, \Theta_0)$  in Eq. 25 for the first scattering event. After a second scattering event,  
 340 the time signal is the convolution of the two time signals  $I_{\phi, d_0}(t, \Theta_0) * I_{\phi, d_1}(t, \Theta_1)$ , and so on.  
 341 When the photon impact the detector, its time signal is convoluted with the chirped pulse signal  
 342 ( $I_p(t, L)$ ). Time signals of all photons reaching the detector are summed together. To decrease  
 343 the memory requirement of such a procedure, we idealize the scattering time signal as a train of  
 344 peaks, *i.e.* a comb, as done in Calba *et al.* [8]. This idealization is based on the fact that when the  
 345 pulse width ( $= c\Delta t$ ) is much smaller than the particle diameter, it acts as a scan in time and angle  
 346 of the particle (see [10]), thus leading to a time signal made of very thin peaks. By virtually  
 347 reducing the pulse duration to a Dirac delta function, it is assumed that the time signal reduces  
 348 to a Dirac comb where peaks are not regularly distributed in time. This method could thus be  
 349 coined the Comb Transport, but is referred to as Method 2 in the following. We are aware that  
 350 this assumption is more a naive geometrical idealization than a real physical argument. One  
 351 could argue, as mentioned above, that the zero area rule must be fulfilled and hence the peaks  
 352 in the time signal could not be thinner than  $2\pi/\omega_0$ . However, because the resulting comb is  
 353 eventually convoluted by the chirped Gaussian pulse (*e.g.*  $I_p(t, z_{\text{detector}})$  in Eq. 25), it is trimmed  
 354 in the frequency domain to the frequency range of the pulse, thus unphysical large frequencies  
 355 are filtered out. Hence its final time representation is equal to the one of the pulse  $> 2\pi/\omega_0$ .  
 356 The comb signal is generated by selecting the peaks of the SSIRF time signal. It is to be noted  
 357 that when the time signal is noisy (for instance when the SSIRF is computed with a varying  
 358 refractive index as seen later), it can be necessary to smooth the time signal. The results of the

359 peak detection is illustrated in Fig. 4. The black line represents the intensity of the time signal at  
 360 forward scattering ( $\theta = 0^\circ$ ) for a droplet in air of size parameter of 100 (left) and 2000 (right)  
 361 illuminated by a laser ( $\lambda_0 = 600$  nm) virtual pulse of two EM cycles. The grey segments are  
 362 the detected peaks. For small particle ( $x = 100$ ), the virtual pulse width becomes closer to the  
 363 particle diameter and the peak identification process misses some peaks. On the contrary for  
 364 large scatterers the time signal is a set of individual and well separated peaks, easing the detection  
 process.

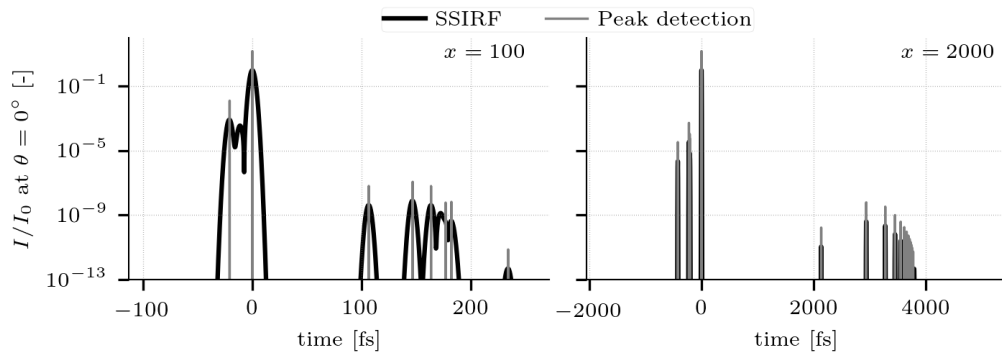


Fig. 4. Time signal at  $\theta = 0^\circ$  for a bubble in water of size parameter 100 (left) and 2000 (right). Black curve is the SSIRF, grey curve are the detected peaks.

365  
 366 The sequence of Method 2 is illustrated in Fig. 5. During a scattering event, the polar angle of  
 367 scattering is randomly drawn as in Method 1. The angle of scattering, to which corresponds  
 368 a given comb, is recorded in a list. When the photon finally impacts the detector, the list of  
 369 scattering angles is converted into a list of combs, which are convoluted recursively. A threshold  
 370 on the amplitude is applied to dismiss weak peaks. The resulting comb is eventually convolved  
 with the time signal of the chirped pulse.

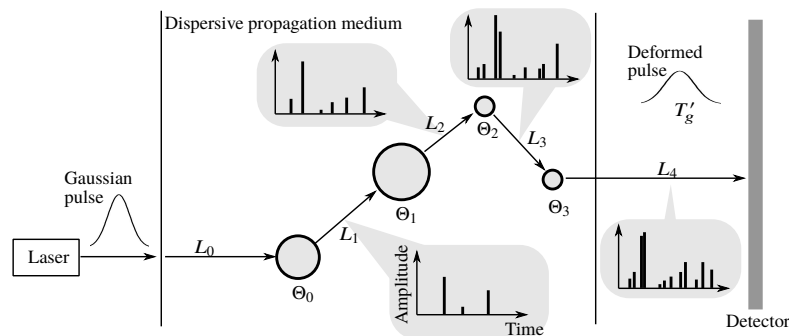


Fig. 5. Sketch of the Comb method.

371  
 372 Method 2 has the advantages of being much lighter in memory because one peak is determined  
 373 by its amplitude and its time and hence requires only two scalars per peak. Also, the discrete  
 374 convolution of a comb is easy to implement with recursion and easy to optimize by sorting the  
 375 peaks by decreasing amplitude. The results of the convolution is that amplitudes are multiplied  
 376 and the times are added. The interested reader is referred to [8] for a detailed explanation on the  
 377 Comb Transport.

378 The results of the two methods will be compared to each other and to other results from literature  
379 in Section 7.

### 380 3.4. Monte Carlo code: Scatter3D

381 The Monte Carlo simulations were performed with the code Scatter3D [21], which was developed  
382 to solve the RTE (Eq. 22) in steady state. Scatter3D can handle advanced optic features such as  
383 fluorescence [22], polarization [23], birefringence [24] or time correlation [25]. Scatter3D was  
384 applied to characterize bioorganic tissues [24] or to predict halftone patterns of ink coverage [26].  
385 One of the particularities of Scatter3D is that it uses a stencil approach where scattering events  
386 are not resolved one by one, but as a group over a given stencil. This is achieved by precomputing  
387 all scattering events for a collection of different scenarii in an elementary volume, and later apply  
388 these possible scenarii. Although this approach can speed up simulations tremendously, this  
389 feature was not used here.

390 The distance between two scattering events  $l_{\text{scat}}$  is drawn from the memoryless exponential law  
391  $e^{-l_{\text{scat}}/l_m}$ , where  $l_m$  is the mean free path length of the photon. The optical thickness  $\tau$  of the  
392 medium is given by  $\tau = l_s/l_m$  where  $l_s$  is the geometrical thickness of the slab.

393 The two methods to compute the scattering transient presented in Section 3.3 were incorporated in  
394 the code. The SSIRF are precomputed by a Python script and processed to provide the  $(t, \theta)$  map  
395 for Method 1 and the comb signal for Method 2. These data are then loaded at the initialization  
396 of Scatter3D. As polydisperse clouds of droplets (or bubbles) are simulated in the following, it is  
397 necessary to precompute the SSIRF for different diameters and load them in Scatter3D. During  
398 the simulation, when a photon impact a scatterer, a diameter is randomly draw from the pool of  
399 precomputed diameters, according to their size distribution.

## 400 4. Spreading of the pulse in water

401 Water is a dispersive optical media and it is important to optimize for pulse length and carrier  
402 frequency to minimize pulse chirping. Absorption by water is also taken into account. Because  
403 of the pulse spectrum broadening, the spreading depends also on the pulse duration. This is  
404 illustrated in the Appendix 9. To quantify the spreading in various conditions, the propagation of  
405 a short pulse in water is simulated according to Eq. 3 for different pulse duration  $\Delta t$  and different  
406 distance to source  $L$ . They are summarized in Table 1. We quantify the pulse spread in space by  
the FWHM of its extension,  $\Delta s$ .

Table 1. Operating parameters for the spreading of the pulse.

$\Delta t$	[fs]	20 - 500
$L$	[mm]	0 - 500

407 In Fig.6 the isolines show the contour of  $\Delta s$ , while the colormaps show the extinction, for different  
408 pulse duration  $\Delta t$  at different depth  $L$  in water, for a carrier wavelength of 400 (left) and 800 nm  
409 (right). The grey dots mark the minimal pulse width for at a given  $L$  found numerically, and the  
410 grey line is the corresponding fitting curve. Since they only shows dispersion, these isolines are  
411 related to the real part of the refractive index. The pulse is much more spread at  $\lambda_0 = 400$  nm than  
412 at 800 nm. This is because the slope magnitude of the real part of the refractive index  $(\partial n/\partial \lambda)|_{\lambda_0}$   
413 at  $\lambda_0 = 400$  nm is much larger ( $-95 \text{ mm}^{-1}$ ) than that at  $\lambda_0 = 800$  nm ( $-17 \text{ mm}^{-1}$ ), which leads  
414 to a larger spreading of the pulse. The key element of Fig. 6 is that there is an optimal pulse  
415 duration to minimize the spread of the pulse at a given distance. Another interesting point from  
416 Fig. 6 is the exponent 0.50 of the fitting correlations, suggesting that the optimal  $\Delta t$  to minimize  
417  $\Delta s$  is proportional to  $\sqrt{L}$ . This highlights the fact that in the current conditions, the real part of  
418

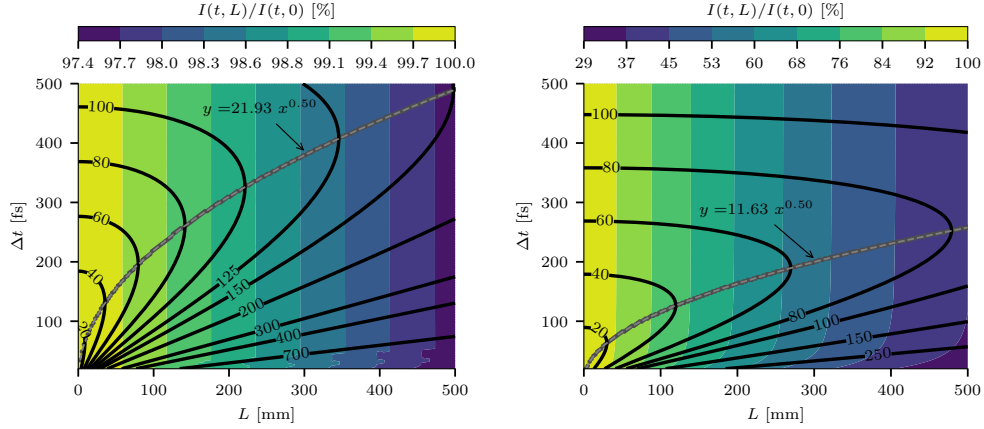


Fig. 6. Map of intensity and isocontours of  $\Delta s$  in micrometer versus the pulse duration  $\Delta t$  and the distance to laser  $L$  for  $\lambda_0 = 400$  nm (left) and 800 nm (right).

419 the refractive index is very well represented by a second order Taylor expansion in  $1/\lambda$ . This is  
 420 demonstrated in the Appendix A.

421  
 422 The maps of extinction here represent the total energy of the pulse normalized by its value at  $z = 0$   
 423 such as  $I(L)/I(0)$  where  $I(L) = \int |X(t, z = L)|^2 dt$ . The much weaker extinction at 400 nm  
 424 compared to that at 800 nm is strongly illustrated with a normalized intensity larger than 97% at  
 425 500 mm whereas the pulse intensity is reduced by two third at 500 mm for  $\lambda_0 = 800$  nm. For  
 426 very short pulses ( $< 70$  fs) at  $\lambda_0 = 400$  nm, the extinction shows non-monotonic variations versus  
 427  $\Delta t$ . This is because the imaginary part of refractive index reaches a minimum at  $\lambda \approx 475$  nm as  
 428 shown in Fig. 17. For very short pulses (*i.e.* 20 fs), the color broadband leads to frequency up  
 429 to 520 nm on the other side of the minimum. But for longer pulses, the maximum wavelength  
 430 reaches the minimum of the extinction, and hence the overall extinction is smaller.

431  
 432 To conclude, when a short ( $< 500$  fs) pulse of visible light propagates in water, the broad-  
 433 band color leads to its spread due to dispersion, and to its weakening due to extinction. It is not  
 434 possible to minimize the pulse spreading and its extinction at the same time. At large wavelengths  
 435 (800 nm), the dispersion effects are lower but the extinction is large, whereas small wavelengths  
 436 (400 nm) are strongly dispersed but very weakly attenuated. However if the water depth is known,  
 437 maps in Fig. 6 are useful to determine the optimal pulse duration. Another solution could be to  
 438 chirp the pulse before it enters the dispersive medium to partly pre-compensate the dispersion.

## 439 5. Sensitivity of the temporal phase function to numerical parameters

440 In this section, we investigate the numerical parameters to accurately compute the scattering  
 441 transient of the real pulse and of the SSIRF, the objective being to find the optimal parameters to  
 442 retrieve Eq. 12. As a first step we assume a non-chirped pulse (non-dispersive medium), so that  
 443 Eq. 12 simplifies to:

$$\psi^s(t, \theta) = g(t) * \phi(t, \theta) \quad (28)$$

444 First we will examine the sensitivity of the LHS to the frequency resolution, then we will use the  
 445 LHS as a reference and examine the sensitivity of  $\phi(t, \theta)$  to satisfy Eq. 28.

446

447 The LHS of Eq. 28 is computed with Eq. 9 for  $L = 0$  and stands as the reference. The

448 reference case consists of a particle of  $x = 500$  size parameter. The FWHM in time of the  
 449 pulse is  $\Delta t = 100$  fs and the wavelength in vacuum of the carrier is  $\lambda_0 = 800$  nm. Two types of  
 450 configurations are studied: (i) a water droplet in air and (ii) an air bubble in water, corresponding  
 451 to a relative refractive index larger and lower than one. The corresponding temporal scattering  
 452 phase functions are illustrated in Fig. 7, where the y-coordinate is expressed in terms of reduced  
 453 time  $t^* = tc_0/(n_{pm}r_s)$ . The different modes of reflection, refraction, and internal reflections are  
 454 discernible even though their overlap. For detailed comments on these maps, the reader should  
 refer to [10].

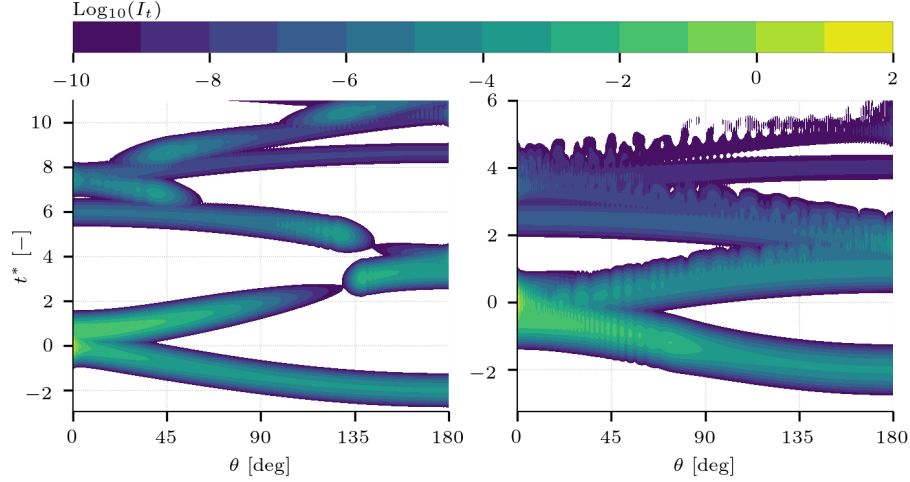


Fig. 7. Transient scattering phase function ( $x = 500$ ) for a water droplet in air (left) and  
 air bubble in water (right) illuminated by a 100 fs and 800 nm laser pulse.

455

### 456 5.1. Time discretization and frequency resolution

457 In the frequency domain, we discretize the frequency axis between  $\omega_{\min}$  and  $\omega_{\max}$  where the  
 458 relative peak of Fourier Transform of the pulse ( $G/G(0)$  in Eq. 1) is larger than a precision  
 459 criterion  $\epsilon$ :

$$459 \omega_{\min}, \omega_{\max} = \omega_0 \pm \Delta\omega/2 \quad \text{where} \quad \Delta\omega = \frac{\sqrt{2 \log(1/\epsilon)}}{\gamma} \quad (29)$$

460 where  $\gamma$  is the time constant such that the temporal signal of the pulse is  $g(t, z = 0) = e^{-(t/\gamma)^2}$   
 461 as given by Eq. 2. Please note the difference of definition between  $\Delta t$  and  $\Delta\omega$ , the former being the  
 462 FWHM *i.e.* Eq. 29 with a precision criterion of  $\epsilon = 0.5$  whereas the latter is the full width for a  
 463 precision criterion  $\epsilon \rightarrow 0$ . The temporal resolution  $dt$  of the signal given by the inverse Fourier  
 464 Transform is:

$$464 dt = \frac{2\pi}{\omega_{\max} - \omega_{\min}} = \frac{2\pi}{\Delta\omega} = \frac{\pi\Delta t}{4\sqrt{\log(2) \log(1/\epsilon)}} \quad (30)$$

465 With  $\epsilon = 10^{-30}$ ,  $dt \approx \Delta t/8.81$ , which means that the largest half of the pulse is resolved by 9  
 466 samples. This is considered here as too coarse, and thus  $\Delta\omega = \omega_{\max} - \omega_{\min}$  will be extended by  
 467 zero padding (and keeping  $d\omega$  constant) in the frequency domain to impose  $dt \approx \Delta t/20$ .

468 The resolution  $d\omega$  of the frequency axis is set by the number of sample  $N_\omega$  between  $\omega_{\min}$  and  
 469  $\omega_{\max}$ , so that  $d\omega = \sqrt{2 \log(1/\epsilon)}/(N_\omega \gamma)$ . Therefore,  $d\omega$ , and hence the accuracy of the transient  
 470 scattering phase function, depend on both the frequency resolution and on the pulse duration,  
 471 due to the presence of  $\gamma$ . Its influence is discussed in the following. After preliminary tests, it

472 was found that the scattering angle where spurious modes are the more prominent is  $0^\circ$ . Thus we  
 473 limit our parameter study to this angle.

474

475 First, we check the influence of the frequency resolution on the real (100 fs, 800 nm) pulse.  
 476 Figure 8 shows the time signal of the scattered intensity  $|\psi^s(t, \theta = 0^\circ)|^2$  for a droplet (left)  
 477 and a bubble (right) illuminated by a real pulse of non-polarized light with different frequency  
 478 resolutions. For the droplet, the background noise is made of spurious modes resulting from the  
 479 discretization of the frequency axis, and decreases as the resolution increases. Concerning the  
 480 physical modes (for  $I/I_0 \gtrsim 10^{-10}$ ), they are predicted with the same accuracy for all  $N_\omega$ . The  
 481 time signal of the bubble (Fig. 8 right) is independent of  $N_\omega$ , highlighting a fast convergence  
 482 with the frequency resolution for the integration of Eq. 9. This suggests a smooth variation of  
 483 the term  $\psi^{cw}(\omega, \theta)$  for a relative refractive index  $m$  lower than one. We consider arbitrarily the  
 484 signal below  $\approx 10^{-12}$  as background noise. The minimum  $N_\omega$  to properly resolve the transient  
 485 of this operating point is 160000 and 40000 for the droplet and the bubble, respectively. We  
 486 will however see in the following that the background noise intensity depends also on other  
 parameters.

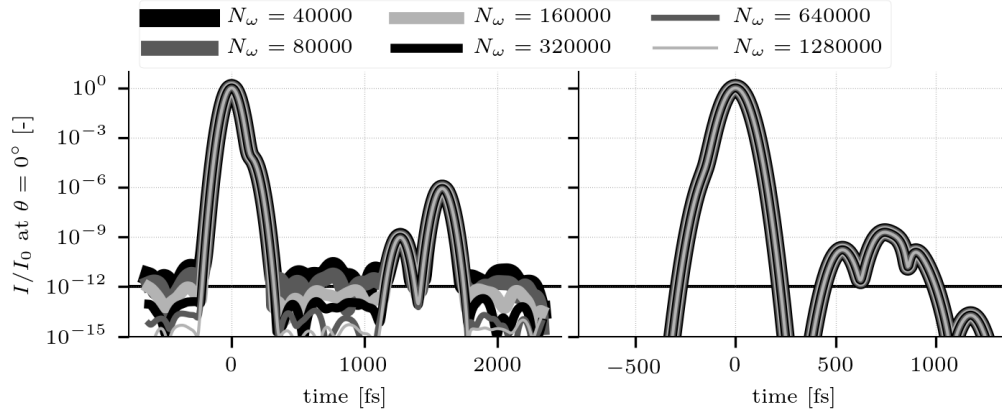


Fig. 8. Time signal at  $\theta = 0^\circ$  for a water droplet in air (left) and air bubble in water (right) illuminated by a 100 fs and 800 nm laser pulse ( $x = 500$ ) computed with various frequency resolutions.

487

## 488 5.2. Computation of the SSIRF with a constant index

489 First we investigate the SSIRF with a constant refractive index for water. The refractive index of  
 490 air is always considered constant. To compute the SSIRF, we resolve Eq. 9 for  $L = 0$  for a virtual  
 491 short pulse of FWHM  $\Delta t_v$  of a few cycles of the carrier such as  $\Delta t_v = \tau_0/2$ ,  $\tau_0$ , and  $2\tau_0$  where  
 492  $\tau_0 = \lambda_0/c_0$ . The frequency resolution is set to  $N_\omega = 1280000$  for all cases. Please note that in  
 493 the case of the SSIRF, the convergence for  $m < 1$  is also faster than for  $m > 1$ , as for the real  
 494 scattering function (Fig. 8). It is however not depicted here.

495

496 All the results are summarized in Fig. 9 whose layout is explained as follows. In the top  
 497 row the intensities of the SSIRFs ( $|\phi(t, \theta = 0^\circ)|^2$ ) for different virtual pulse durations  $\Delta t_v$  are  
 498 shown for the droplet (left) and bubble (right). The transient scattered intensity for a real pulse  
 499 ( $\Delta t = 100$  fs) is given for comparison purpose in thick black line. In the bottom row of Fig. 9 the  
 500 SSIRFs are convolved with an ideal Gaussian pulse of  $\Delta t = 100$  fs and the resulting intensity is  
 501 compared to the one of the real pulse.

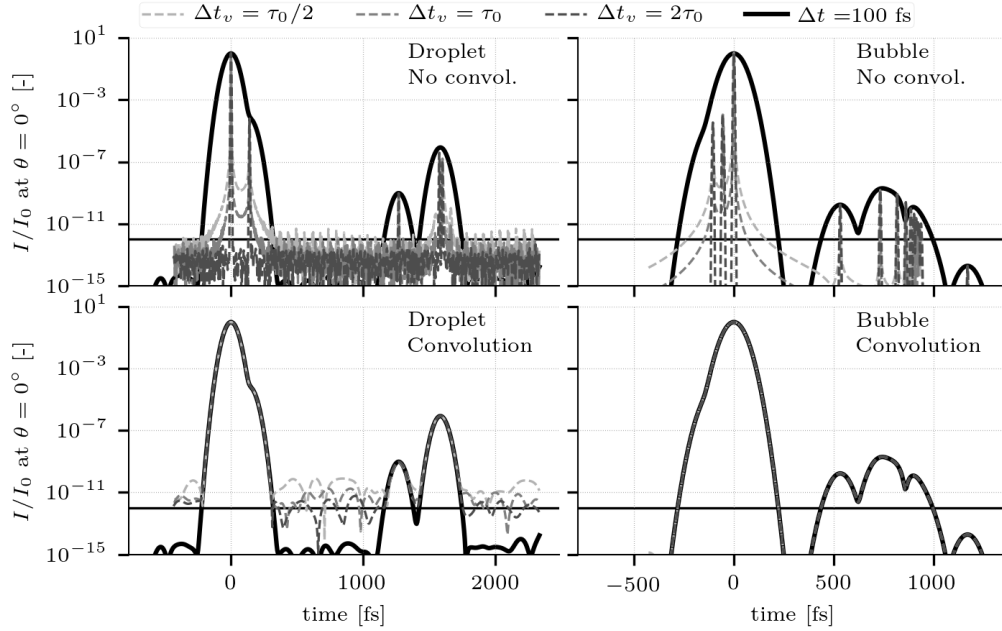


Fig. 9. Time signal of the smoothed SIRF at  $\theta = 0^\circ$  for a water droplet in air (left) and air bubble in water (right) illuminated by a 800 nm laser pulse of duration  $\tau_0/2$ ,  $\tau_0$ ,  $2\tau_0$ , superimposed with the transient scattering function of the same particles illuminated by a 100 fs pulse. Top: original SSIRF. Bottom: SSIRF convoluted the 100 fs pulse. Refractive indices are constant.

502 First, we discuss the non-convolved SSIRF (Fig. 9 top). It is observed with the droplet configura-  
503 tion that the intensity of the spurious modes depends also on  $\Delta t_v$  ( $\equiv \gamma$ ) as mentioned above,  
504 because  $d\omega$  is inversely proportional to  $\Delta t_v$ . Another striking effect is that for  $\Delta t_v \leq \tau_0$ ,  
505 the signal around the primary peaks (around  $t = 0$  fs) raises above  $10^{-12}$  in the approximate shape  
506 of a Laplace distribution with large tails. This is particularly visible for the bubble. This effect is  
507 independent of  $N_\omega$ , and is attributed to a non-physical artifact such as the violation of the "zero  
508 area" rule when  $\Delta t_v < \tau_0$ . Interestingly this effect has no influence on the convoluted signals  
509 (Fig. 9 bottom), where the matching between the real signal and the convoluted signal is perfect  
510 for the bubble, most presumably because of the frequency trimming. For the convoluted signal  
511 of the droplet, the agreement is excellent on the peaks, but the intensity of the spurious modes  
512 depends on  $\Delta t_v$  and decreases when  $\Delta t_v$  increases. The good agreement on Fig. 9 (bottom)  
513 validates the present approach (Eqs. 12 and 28).

### 514 5.3. Computation of the SSIRF with dispersion

515 In this part the dispersion and extinction are taken into account in the computation of the SSIRF.  
516 The scatterer is virtually located at the source ( $L = 0$ ), so that the pulse is not chirped, but the  
517 term  $\psi^{cw}(\omega, \theta)$ , which depends on the relative refractive index has an additional dependency on  
518  $\omega$ .

519 In order to take the dispersion and extinction into account, it is necessary to know the variation of  
520 the refractive index over the whole range of wavelength. In the case of a real pulse, the broadband  
521 color is well included in the range where the index of water was accurately determined in the  
522 literature (see Fig. 17). However in the case of a virtual pulse, the broadband color is much  
523 larger with a wavelength ranging from 148 nm to the infinity in the present conditions. Hence,

524 in this part we created a hybrid model by combining the databases from Harvey *et al.* [27] and  
525 Segelstein [28] for the real part of the refractive index of water. This is motivated by the fact that  
526 the results from Segelstein [28] (i) deviate substantially from other more measurements of the  
527 literature [29–31] for visible light and (ii) are the only measurements for extreme wavelengths.  
528 The details of this hybrid model are given in Appendix B.

529 All the results are gathered in Fig. 10 whose layout is identical to that of Fig. 9. The first  
530 comments are on the transient of the real pulse ( $\Delta t = 100$  fs). Dispersion in water has a weak  
531 influence on the real pulse signal in the two cases because the diameter of the scatterer ( $\approx 100 \mu\text{m}$ )  
532 is much smaller than the distance over which the pulse spreads significantly (see Fig. 6). This  
533 results suggests that at the scale of the scatterer, the pulse spreading could be neglected and hence,  
534 the SSIRF could be computed with a constant refractive index. The influence of dispersion  
535 and extinction on the SSIRF is very strong for both the droplet and the bubble, especially for  
536  $\Delta t_v \leq \tau_0$  where the unconvolved (top) time signals show an unacceptable large background  
537 noise far above the transient signal of the 100 fs pulse. Despite this very distorted signal for  
538 the SSIRF, when it is convolved with the pulse, it matches the transient of the real pulse very  
539 well (bottom). Again, this very good agreement is explained by the fact that the very noisy time  
540 signal of the SSIRFs is due to the large variations of the refractive index over the unrealistic  
541 large range of  $\lambda$ . However the convolution with the pulse act as a frequency filtering to keep  
542 only the frequencies of the pulse, where the refractive index does not vary much, hence the  
543 good agreement. This point also shows that even though the SSIRF computed with  $\Delta t_v < \tau_0$   
544 does not represent any physical phenomenon because of the zero-area rule, its convolution  
545 with the realistic signal of the pulse leads to a realistic results because the convolution filters  
546 out unphysical artifacts of the SSIRF. Additional test were performed with  $\Delta t_v = \tau_0/4$  and  
547  $\tau_0/8$  and the agreement was always very good. Hence the SSIRF computed with  $\Delta t_v < \tau_0$   
can be considered as non-real object that needs to be convolved in order to carry a physical signal.

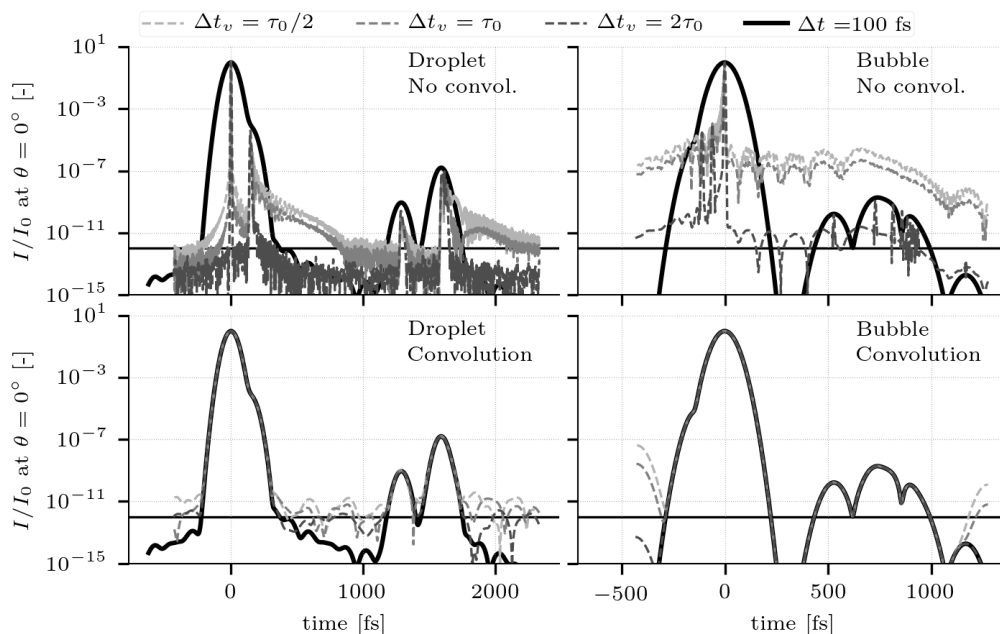


Fig. 10. Same legend as Fig. 9 except that water refractive index depends on the wavelength.

550 Finally, the SSIRF is illustrated in Fig. 11 for a scatterer of  $100\ \mu\text{m}$  for constant refractive  
 551 indices and  $\Delta t_v = 2\tau_0$ . The case of a water droplet in air (left) was resolved with a total resolution  
 552 (including zero padding)  $N_\omega$  of 2380337 while the case of air bubble in water (right) was resolved  
 with  $N_\omega = 595085$ . The better convergence of bubble is clearly visible.

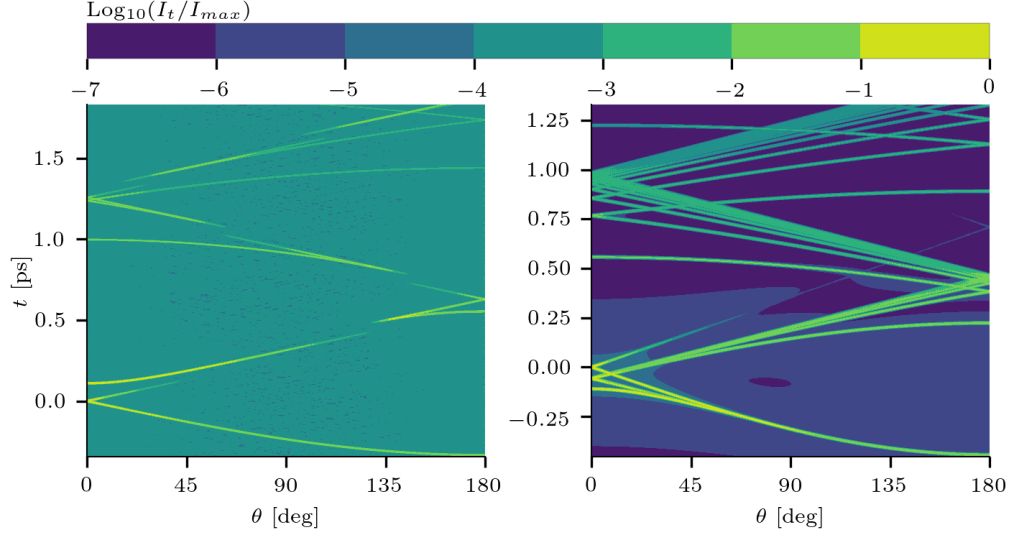


Fig. 11. Map of the SSIRF for a scatterer of  $100\ \mu\text{m}$  ( $x \approx 500$ ). Droplet (left) and bubble (right).

553 To conclude on this part, the SSIRF-based approach was shown to provide a very good transient  
 554 time signal.  
 555

## 556 6. Validation of transient single scattering with the energy approximation

557 In this part we verify that the SSIRF approach also works with the energy approximation, with  
 558 the two methods discussed earlier. Also, we verify that the approaches work with a chirped  
 559 pulse, *i.e.* when the scatterer is located at a distance  $L$  from the laser source. We only study air  
 560 bubbles in water in this part. To validate the approaches, we use the intensity given by the exact  
 561 transient scattered field of a chirped pulse after one scattering event (squared modulus of Eq. 9)  
 562 as a reference, and we compare the methods expressed by their intensity time signal. For the full  
 563 Monte Carlo method (Method 1), it consists in randomly drawing a large number of scattering  
 564 time (Eq. 26b). In the present case of single scattering, the time at which the scattered photon  
 565 reaches the virtual detector (shown in Fig. 1) is:

$$T_I|_{(L, \Theta_0)} = T_{g'}|_L + T_0|_{\Theta_0} \quad (31)$$

566 which is the summation of the random time due to the pulse chirped after a distance  $L$  and the  
 567 random time due to the scattering in the direction  $\theta$ . The intensity is given by the histogram of  
 568  $T$ . The PDF of  $T_{g'}|_L$  is given by the intensity of the chirped pulse  $I_p(t, L) = |g'(t, L)|^2$  where  
 569  $g'(t, L)$  is computed from Eq. 5. The random variable  $T_0|_{\Theta_0}$  follows the PDF given by the energy  
 570 of the SSIRF  $|\phi_S(t, \Theta_0)|^2$  (Eq. 15) with a duration  $\Delta t_v$  of two cycles ( $2\tau_0$ ).

571 For Method 2, the intensity is given by Eq. 25, which in this case simplifies to:

$$I(t, \theta, L) \approx I_p(t, L) * I_\phi(t, \theta) \quad (32)$$

572 where  $I_p(t, L)$  is the energy of the chirped pulse and  $I_\phi(t, \theta)$  is the time signal of the SSIRF  
 573 with the comb representation. We will show that detecting the peaks from the SSIRF computed

574 with a constant index (non-dispersive medium) is preferable than in a dispersive medium. Indeed  
 575 as shown earlier, the SSIRF computed with dispersion is usually noisier and more cumbersome  
 576 to detect peaks. This approximation is also justified if the dimension of the bubbles are smaller  
 577 than the characteristic length of the pulse spreading, *i.e.* when the incident wave does not spread  
 578 much between the two boundaries of the bubble. This result is important because it removes the  
 579 necessity to characterize the refractive index over a large range of wavelengths.

580 Figure 12 compares the time signals based on Eq. 31 with the SSIRF computed in dispersive  
 581 and non-dispersive medium, for different  $L$  in the forward ( $\theta = 0^\circ$ ) direction. Each curves is  
 582 based on one billion samples. The major peak around  $t = 0$  is well predicted for all  $L$ . The  
 583 secondary peaks at  $t < 0$  are in acceptable agreement for  $L = 0$  mm but they are less and less  
 584 resolved as  $L$  increases. Because of the very large amplitude ratio ( $\approx 10^{-9}$ ) between majors  
 585 and secondary peaks at  $t > 0$ , several tens of billions samples would be necessary to reach statistical  
 586 convergence for all peaks, which was not done here, and thus they are not captured. This is  
 especially detrimental at  $L = 0$  and 100 mm where the secondary lobes are particularly visible.

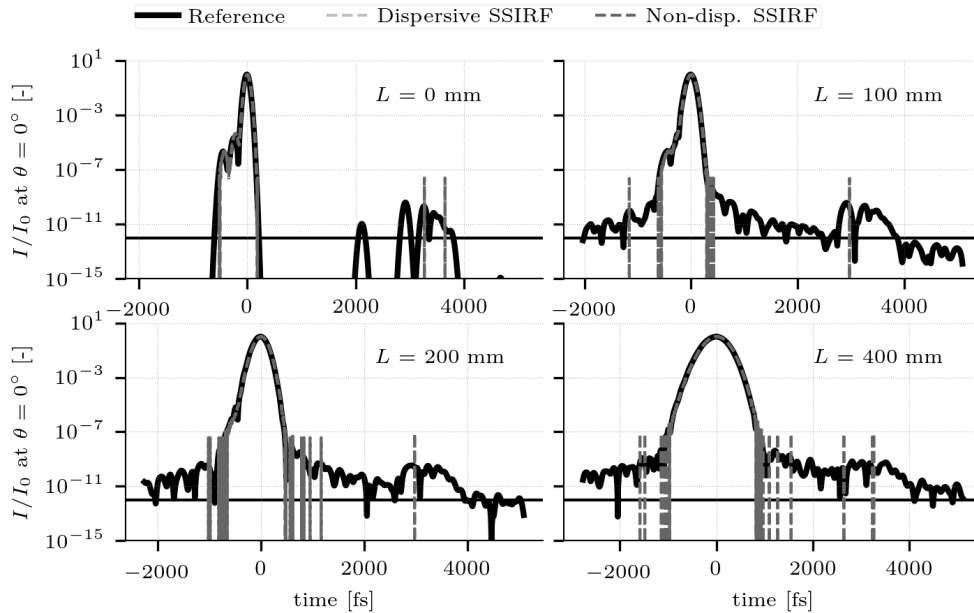


Fig. 12. Time signal at  $\theta = 0^\circ$  for bubbles ( $x = 2000$ ) at different distances  $L$  from the laser source with Method 1. The SSIRF was computed with varying (light grey curve) and constant (dark grey curve) dispersive index.

587  
 588 Figure 13 compares the time signals based on Eq. 32 in the same condition as for Fig. 12. In  
 589 this case, the agreement is very good for all distances. The secondary peaks at  $t > 0$  are well  
 590 captured up to  $L = 200$  mm, which is an advantage over Method 1. However as for Method 1  
 591 the resolution of the secondary peaks at  $t < 0$  decreases as  $L$  increases. The results are slightly  
 592 better with the non-dispersive SSIRF because more peaks are captured.

## 593 7. Transient multiple scattering with the energy approximation

### 594 7.1. Comparison with results from literature

595 The results of Method 2 are compared with those of [8] where the authors used the energy  
 596 approximation with the Comb Transport (our Method 2) to simulate the transient scattering of a

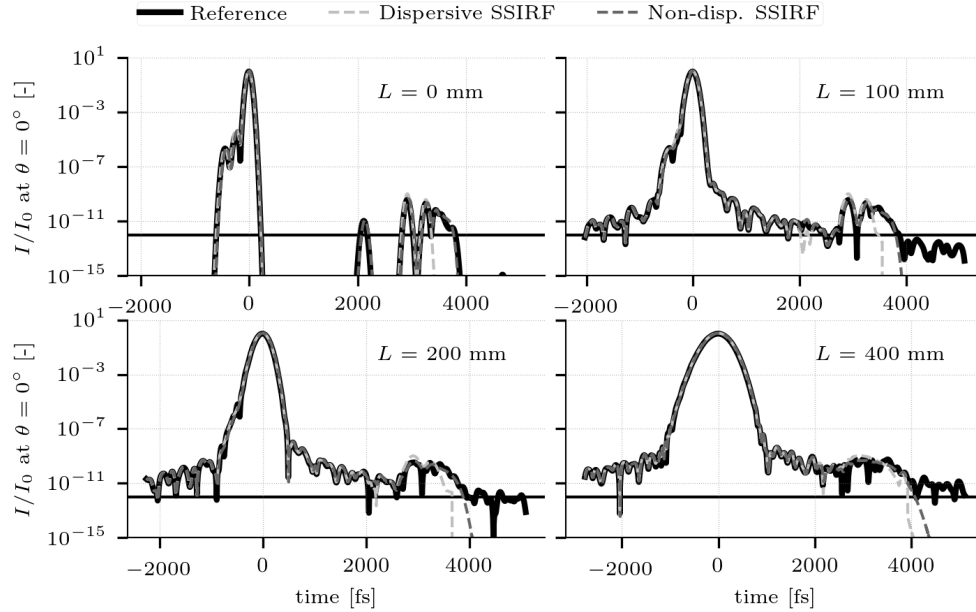


Fig. 13. Time signal at  $\theta = 0^\circ$  for bubbles ( $x = 2000$ ) at different distances  $L$  from the laser source with Method 2. The SSIRF was computed with varying (light grey curve) and constant (dark grey curve) dispersive index.

597 polydisperse cloud of water droplets in air. The notable difference with the present approach is  
 598 that they used the Debye expansion, and not the LMT, to create the comb time signal. There are  
 599 several advantages to use the Debye expansion over the LMT. First, it requires less discretization  
 600 points in the frequency domain to reach the same convergence for Eq. 9, provided that enough  
 601 modes are computed ( $\approx 20$ ). The authors report a number of point of  $2^{11}$  for the Debye expansion  
 602 versus  $2^{18}$  for the LMT to reach the same accuracy. Second, it is easier to detect peaks because  
 603 each Debye mode is expressed as an individual time signal. Therefore different peaks of different  
 604 refraction modes do not interfere or merge with each other. Third, because each peak is associated  
 605 to an order of refraction, it is possible to interpolate the amplitude and time of each refraction  
 606 mode with regards to the angle of scattering and the droplet diameter. For instance if the set  
 607 of randomly drawn diameter and angle  $(d, \theta)$  is included in the square (in the parameter space)  
 608 delimited by  $(d_i, \theta_i)$  and  $(d_{i+1}, \theta_{i+1})$ , then the amplitudes and delays of the peaks for each mode  
 609 can be interpolated. With the LMT, because all modes are gathered in a single time signal, they  
 610 cannot be easily identified, and hence the peaks cannot be interpolated. The major drawbacks of  
 611 the Debye expansion is that it does not converge in case of relative refractive index smaller than  
 612 one (*e.g.* air bubble in water), in the vicinity of the critical angle. This is the reason why the  
 613 present study relies on LMT.

614 As in the present study, the strategy in [8] is to precompute the scattering phase functions that are  
 615 used to randomly draw the scattering direction of photons. The polar angle was discretized on a  
 616 grid of  $d\theta = 0.01^\circ$  resolution between  $0$  and  $1^\circ$ , and then  $d\theta = 1^\circ$  up to  $180^\circ$ . It was verified (but  
 617 not presented here) that for scattering angles of  $0$  and  $90^\circ$  the time signal given by the Debye  
 618 expansion in [8] matches the one of the LMT in the present study.

619 The configuration studied in [8] is a slab of thickness  $10$  cm in the laser direction and of infinite  
 620 extent in the other directions. The parameters of the reference case are as follows. The slab

621 contains a polydisperse spray of water droplets in air, and is illuminated by a laser ( $\lambda_0 = 600$  nm)  
622 pulse of FWHM 50 fs. The droplet size distribution is given by a Gaussian function of mean  
623  $100\ \mu\text{m}$  and width  $\delta d$  at  $e^{-1}$  of  $5\ \mu\text{m}$ , and the optical depth is 8. A circular detector of diameter  
624  $5\ \text{mm}$  is located on the optical axis of the laser at  $20\ \text{cm}$  from the slab.  
625 Since Calba *et al.* [8] use the Comb Transport approach, we compare first their results with our  
626 Method 2 implemented in the code Scatter3D. All simulations in the present paper are performed  
627 with one billion photons. The authors conducted several parametric studies which are used here  
628 for validation and presented in Fig.14 where the intensity on the detector is normalized by its  
maximum and plotted versus time.

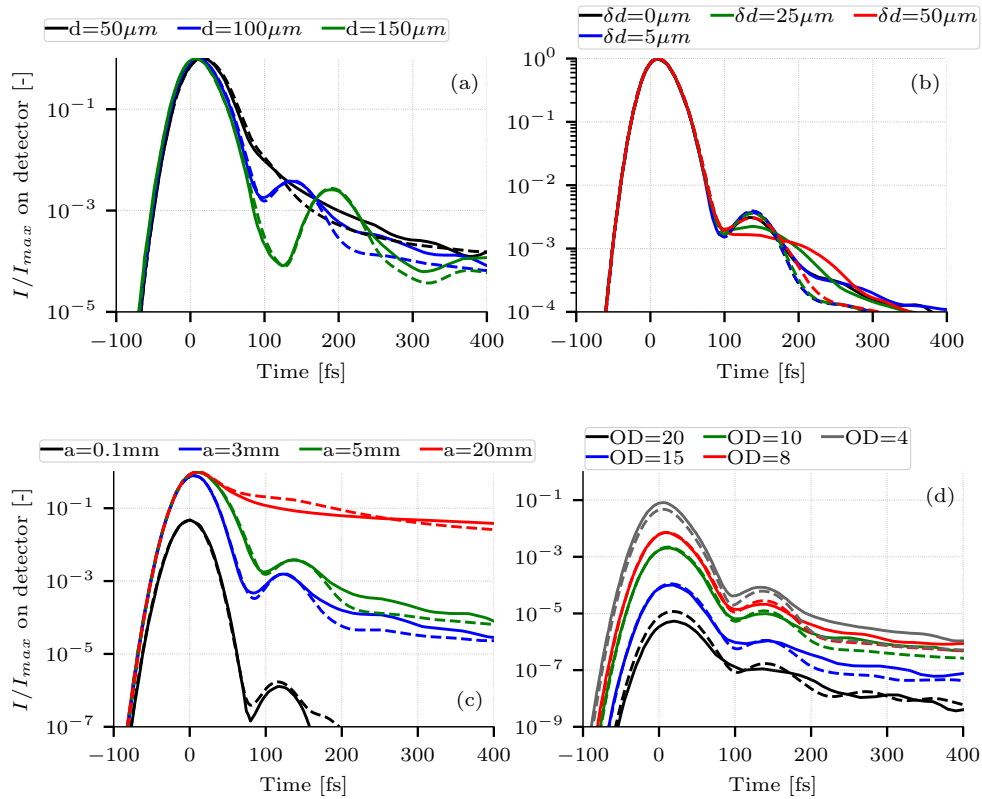


Fig. 14. Intensity on the detector for different mean diameters (a), polydispersity (b), detector sizes (c) and optical thickness (d). Plain lines are from [8], dashed lines are from the present Method 2. Reference droplets cloud is polydisperse with a Gaussian distribution of mean  $100\ \mu\text{m}$  and width  $5\ \mu\text{m}$ .

629 Plain and dashed lines correspond to the results of [8] and our results, respectively. The time  
630 reference ( $t = 0$ ) is the one of ballistic photons reaching the detector. The parameter studies were  
631 performed on the mean diameter of the spray (a), its polydispersity (b), the optical thickness (c)  
632 and the detector size (d). The global shape of the curves is a smooth peak of highest amplitude  
633 followed by a second weaker one. As shown in [8], the first peak corresponds to ballistic (not  
634 scattered) and snake (only diffracted) photons, which explain why the first peak occurs slightly  
635 later than  $t = 0$  fs. The second peak is due to photons that underwent one refraction and multiple  
636 diffractions. These peaks are always well captured in time and amplitude by our method, thus  
637 proving that phenomena of ballistic, snake and refracted photons are accounted with the same  
638

639 accuracy as in [8]. In addition, our parameter studies match those of [8] for the mean diameter, the  
640 optical thickness and the detector size, thus ensuring an equivalent treatment of these parameters.  
641 The discrepancy for the study on polydispersity is for now not clear. To rule out any mistakes  
642 from the present model, it is demonstrated in the Appendix C that the diameter distribution is  
643 correctly taken into account.

## 644 7.2. Comparison of the two methods with droplets and bubbles

645 Method 1 and Method 2 presented here are compared to each other in the same configuration as  
646 the previous section, for different mean diameters. They are shown in Fig. 15 (left) where the  
647 intensity is in arbitrary units proportional to the detected number of photon. The first peak is  
648 larger for larger particles because of their larger cross section. The prediction of the first peak  
649 is in agreement with only a slight shift in time of a few femtoseconds. Except for the primary  
650 peak, the time signal of Method 1 is noisier than the one of Method 2, due to the lower statistical  
651 convergence inherent to Method 1. Discrepancies are observed for the secondary peak with a  
652 shift in the amplitude, which means that in Method 1 the relative probability to have a refraction  
653 against having a diffraction in the forward direction is underestimated. Since both methods are  
654 based on the same computation of the SSIRF, the underestimation does not come from the SSIRF  
655 approach, but from the method itself. For larger time ( $t > 300$  fs), both methods match again,  
656 which suggests that the discrepancy lies in the way the method distribute in time the energy due  
657 to refraction.

658 The same simulation was performed while inverting liquid and gaseous phase, hence simulating a  
659 polydisperse cloud of bubbles in water. Dispersion was not taken into account. Results are shown  
660 in Fig. 15 (right). First, we describe the differences with the water droplets case where the first  
661 peak is the result of ballistic and snake photons while the next peaks are due to refracted photons.  
662 In the case of bubbles, the first peak to appear is the one attributed to photons which underwent  
663 only one refraction and any number of diffractions. This is because photons travel faster in air  
664 than in water, so that refracted photons travel faster than diffracted photon, as observed in single  
665 scattering simulation [10]. Other peaks earlier than  $-200$  fs were also observed (but not reported  
666 here) with an intensity  $< 10$ . These are attributed to multiple refractions and any number of  
667 diffractions, which reduce further the time of flight of the photon. The peak due to ballistic and  
668 snake photons only has still the largest amplitude and appears later. After that, the time signal  
669 contains no significant information. Concerning the comparison of the two methods, the case  
670 of bubble allows to separate two effects. First, the tail of the largest peak decreases faster with  
671 Method 1 compared to Method 2, which again suggests that Method 1 over promotes diffraction.  
672 Second, the refraction peaks are predicted at the same time for the two methods while their  
673 amplitude is different, which confirm that Method 1 underestimates the relative probability of  
674 refraction in forward direction.

675 Concerning computational overheads, Method 2 is more expensive because of the discrete  
676 convolution on peaks for each photon whereas Method 1 only draw random times. However,  
677 since the precomputed table are discretized in time for Method 1 whereas only peak time location  
678 are saved in Method 2, Method 1 is extremely memory intensive compared to Method 2. For  
679 instance the results of Method 1 were obtained by discretizing the time over 5000 elements,  
680 resulting in precomputed tables of 46 MB versus 124 KB for Method 2. This large amount of  
681 memory can significantly slow the computation with Method 1, even more than with Method 2.  
682 With a case presented in this section, with the polydispersity discretized on 31 diameters (*i.e.* 31  
683 precomputed tables) and time discretized over 5000 elements, Method 1 was 13% slower than  
684 Method 2.

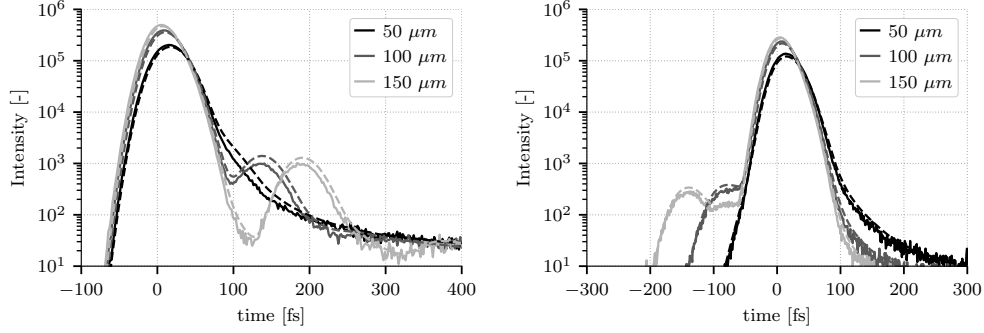


Fig. 15. Comparison of the Monte Carlo approach (plain line) with the comb approach (dashed line) for different mean droplet (left) and bubble (right) diameters.

## 8. Scattering through a bubbly flow with pulse dispersion

In this section we illustrate the effect of the pulse spreading due to beam chirping in a more realistic configuration. The laser wavelength is set to 800 nm, the slab thickness is 100 mm. According to Fig. 6, we choose a pulse duration  $\Delta t = 100$  fs to minimize the pulse spread for a pathlength of 100 mm. We assume the bubble size distribution is Gaussian with mean  $d = 500 \mu\text{m}$  and standard deviation  $\delta d = 100 \mu\text{m}$ . As in the previous section, we also investigate the influence of mean diameter and polydispersity on the time signal. The detector is as previously a disk of 5 mm diameter located at 200 mm from the slab.

To take the pulse spreading into account, we precompute the pulse spread  $\Delta s(\Delta t, L)$  for an optical path length ranging from the minimum slab thickness 100 to 500 mm which we load into Scatter3D. When the photon reaches the detector the optical path length is converted into the pulse spread. For Method 1, the random variable of the pulse delay  $T_{g'}|_L$  (see Eq. 26) is drawn according to a normal distribution whose variance is directly related to the spread. For Method 2 we make a simplification. In principle, the total time signal on the detector is the summation of all photons, whose individual time signal is convolved by the chirped pulse. Hence, summing Eq. 25 on all photons reaching the detector writes:

$$I_{\text{detector}}(t) = \sum_{\text{photons}} \left( I_p(t, L) * \bigotimes_i I_{\phi, d_i}(t, \theta_i) \right) \quad (33)$$

In the present configuration, since the angle resolution of the detector is rather small ( $\Delta\theta \approx 0.712^\circ$ ), photons of similar time of arrival on the detector have a similar optical path length  $L$  and hence a similar pulse spread  $\Delta s$ . In other words the photons that reach the detector at time  $t$  belong to a pulse of mean spread  $\Delta s_m(t)$ . This allows us to take the convolution by  $I_p(t, L)$  out of the summation in Eq. 33. Therefore, when the photon reach the detector its time signal is not convolved by the chirped pulse, but directly summed up with other photons. Also, we record the mean pulse spread  $\Delta s_m(t)$  for each  $t$ , weighted by the peaks amplitude. At the end of the simulation, the time signal is a very dense comb, that we convolve with the locally chirped pulse:

$$I_{\text{detector}}(t, \theta, L) \approx \int_{t_{\min}}^{t_{\max}} S(\tau) \cdot I_p'(t - \tau, \Delta s_m(t)) d\tau$$

where  $S(\tau) = \left( \sum_{\text{photons}} \bigotimes_i I_{\phi, d_i}(\tau, \theta_i) \right)$  (34)

709 and  $I'_p(\tau, \Delta s_m(t))$  is the chirped pulse intensity of spread  $\Delta s_m(t)$  at time of arrival  $t$ . Note that  
 710  $S(\tau)$  is the dense comb obtained at the end of the simulation.

711

712 The parameter studies on the mean diameters is shown in Fig. 16 (top left) with the two  
 713 methods where their curves of same color match very well. As in the previous section, ballistic  
 714 and snake photons carry most of the energy and reach the detector after the refraction photons.  
 715 Two peaks for  $d = 400$  and  $500 \mu\text{m}$  are observed prior to the no-refraction mode. The earliest one  
 716 corresponds to  $p = 1$  mode of the Debye expansion while the second corresponds to other  $p > 2$   
 717 modes as explained in [10]. These two peaks in forward direction are also visible in the illustration  
 718 of the SSIRF for bubbles (Fig. 11 right). The influence of dispersion is illustrated in Fig. 16  
 719 (bottom left) where extreme cases ( $d = 300$  and  $500 \mu\text{m}$ ) are shown with and without dispersion.  
 720 The influence of the pulse spread is stronger for thinner peaks (e.g. main peak) and almost  
 721 negligible for wider peaks (e.g.  $p = 1$  peak). For  $d = 300 \mu\text{m}$  the  $p > 2$  peak is merged to the main  
 722 peak. Therefore, when the pulse spread increases (e.g. for a thicker slab) the different refraction  
 723 modes could be less distinguishable. The parameter study on the polydispersity is shown in  
 724 Fig. 16 (top right) for Method 2 only. The general trend is that wider diameter distributions lead to  
 725 smoother time signals, thus diminishing the contrast of the refraction modes. The same effects due  
 726 the pulse spread is observed. Note that in our representation the influence of extinction is neglected.

727

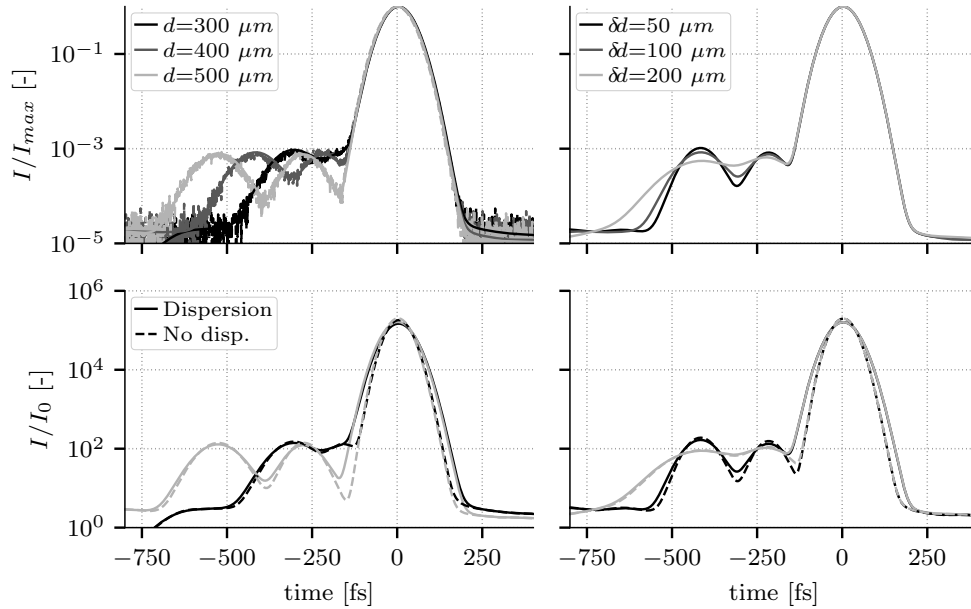


Fig. 16. Top left: Comparison of the Monte Carlo approach (plain line) with the comb approach (dashed line) for different mean droplet diameters. Top right: Comb approach for different polydispersity at mean diameter  $400 \mu\text{m}$ . Bottom: influence of dispersion for  $d = 300$  and  $500 \mu\text{m}$  (left) and  $\delta d = 50$  and  $200 \mu\text{m}$  (right)

728 To conclude this part, the mean diameter of the bubble cloud influences the temporal position of the peaks while the width of the diameter distribution acts on the width of the refraction modes. As for the previous results on droplets claimed by [8], the characterization of the bubble cloud could be obtained from the time signal, with an appropriated analysis depending on the exact configuration, and on unknown parameters. Note that concentration and optical depth also

733 influence the peaks amplitudes and their width.

## 734 **9. Conclusion**

735 In this paper a model of the transient of multiple scattering in a dispersive medium was presented  
736 in terms of EM wave amplitude and turned to intensity. The model is more generic than the  
737 current state of the art because it relies on the Lorenz-Mie Theory and hence allows to consider  
738 clouds of scatterers of relative refractive index lower than one, typically air bubbles in water. It  
739 can be further extended to take polarization into account.

740 We showed that the scattering effect can be decoupled from the pulse generation and propagation  
741 and hence it can be modeled individually by the Scattering Impulse Response Function (SIRF).  
742 The SIRF can be accurately approximated by a smoothed expression (SSIRF) to detect the peaks  
743 in the time-direction map. The SSIRF was turned into an energy form to be incorporated in the  
744 Radiative Transport Equation. The maps of the pulse spread and extinction were drawn for ultra  
745 short pulse propagating in water, and an analytical expression for the pulse spread was given  
746 and validated for visible light. Two methods to account for the transient were investigated in the  
747 framework of Monte Carlo simulation. The first being a naive Monte Carlo approach, where  
748 scattering delays are randomly drawn, the second being the transport of the time signal of the  
749 scattering transient. It was found that even slightly more complex to program, Method 2 is much  
750 more efficient in terms of resolution, statistical convergence, time of execution and memory  
751 consumption. Therefore the authors strongly advise the use of Method 2. The two methods were  
752 validated against previous numerical simulations from the literature. When applied to the case of  
753 multiple scattering by a cloud of bubbles in water, it was shown that the scattered photons exit the  
754 medium earlier than ballistic and snake photons, and even that different peaks occur for photons  
755 undergoing a different number of refraction. These results open the door for new diagnostics  
756 based on ultrashort laser pulse to characterize bubbly flows.

## 757 **Funding**

758 The authors acknowledge the support of the US Office of Naval Research (N000141712616)  
759 under the supervision of Drs. Thomas Fu and Woei-Min Lin, and the US Department of Energy  
760 (DE-NE0008747).

## 761 **Appendix A: Details on pulse spreading in water**

762 We plot the real (thick plain blue line) [27] and the imaginary (thick plain red line) [28] part of  
763 water refractive versus the wavelength in Fig. 17. We overlay the spectrum boundaries (vertical  
764 lines) of a light pulse for various duration  $\Delta t$ , with a central wavelength at 400 (dotted lines)  
765 and 800 nm (dashed lines). These wavelengths correspond to a doubled and single frequency  
766 Ti:Sapphire laser, respectively. The grey dotted, and dashed non vertical lines are second order  
767 Taylor expansion of the real part, they are discussed later.

768 First, the wavelength boundaries are not equally centered around  $\lambda_0 = 2\pi/\omega_0$  because the  
769 wavelength is inversely proportional to  $\omega$ :  $\lambda = 2\pi c/(\omega_0 \pm \Delta\omega)$ , so that the small frequencies  
770  $\omega_{\min}$  dramatically increase  $\lambda_{\max}$ , as particularly visible with  $\Delta t = 20$  fs. Shorter pulses lead to  
771 larger wavelength ranges, and hence to larger dispersion which eventually lead to larger pulse  
772 spreading. Concerning the extinction for  $\lambda_0 = 800$  nm, it increases by more than two orders of  
773 magnitude from 1000 to 1400 nm, so that the intensity of pulses below 70 fs are more damped as  
774 visible in Fig. 6. In the case of  $\lambda_0 = 400$  nm, the extinction is almost two orders of magnitude  
775 smaller for all investigated pulse duration compared to the extinction at 800 nm, hence the larger  
776 propagated intensity (Fig. 6).

777  
778 In order to demonstrate that the optimal  $\Delta t$  to minimize  $\Delta s$  is proportional to  $\sqrt{L}$ , we ex-

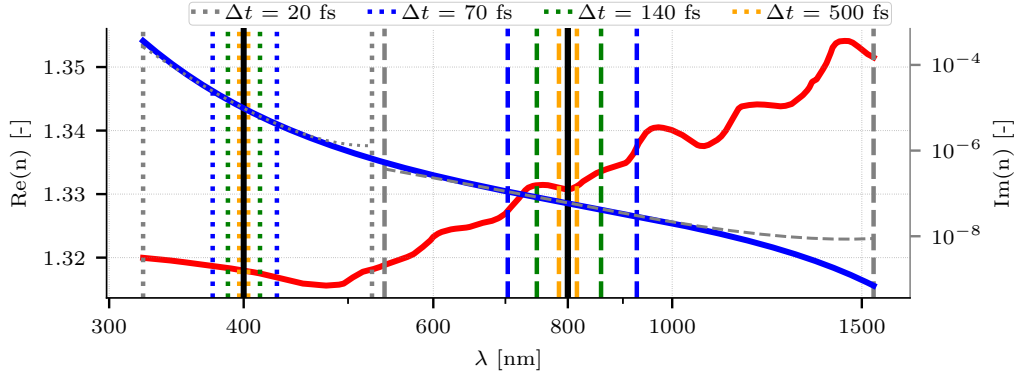


Fig. 17. Real (thick plain blue line) [27] and imaginary (thick plain red line) [28] part of water refractive versus the wavelength. Vertical lines show the spectrum boundaries for various duration at  $\lambda_0 = 400$  (dotted lines) and 800 nm (dashed lines). Grey dotted, and dashed non vertical lines are second order Taylor expansion of the real part, centered at  $\lambda_0 = 400$  and 800 nm.

779 press the dispersion not as  $n(\lambda)$ , but as  $k(\omega)$ ,  $k$  being the wavenumber. This is equivalent, and  
 780 more appropriate for wave propagation. A Taylor expansion of  $k$  at  $\omega_0$  to the second order gives:

$$k(\omega) \approx k_0 + k'_0(\omega - \omega_0) + \frac{1}{2}k''_0(\omega - \omega_0)^2 \quad (35)$$

781 where

$$k_0 = k(\omega_0), \quad k'_0 = \left. \frac{dk}{d\omega} \right|_{\omega_0} \quad \text{and} \quad k''_0 = \left. \frac{d^2k}{d\omega^2} \right|_{\omega_0} \quad (36)$$

782 Note that Eq. 35 can be expressed in term of  $n(\lambda)$  by:

$$k_0 = \frac{2\pi}{\lambda_0}n_0, \quad k'_0 = \frac{n_0}{c_0} \left( 1 - \lambda_0 \frac{n'_0}{n_0} \right) \quad \text{and} \quad k''_0 = \frac{\lambda_0^3}{2\pi c_0^2}n''_0 \quad (37)$$

783 where  $n_0$ ,  $n'_0$  and  $n''_0$  have the same definition as in Eq. 36 by substituting  $(k, \omega)$  with  $(n, \lambda)$ :

$$n_0 = n(\lambda_0), \quad n'_0 = \left. \frac{dn}{d\lambda} \right|_{\lambda_0} \quad \text{and} \quad n''_0 = \left. \frac{d^2n}{d\lambda^2} \right|_{\lambda_0} \quad (38)$$

784 One can show that if the original non-chirped pulse is expressed in the time domain as  $e^{-(t/\gamma_0)^2}$ ,  
 785 the actual time constant  $\gamma(z)$ , representative of the spread in time of the pulse at coordinate  $z$  is  
 786 expressed as [32]:

$$\gamma(z)^2 = \gamma_0^2 + \left( \frac{2k''_0 z}{\gamma_0} \right)^2 \quad (39)$$

787 As the spread in space of the pulse is proportional to the spread in time, minimizing the spatial  
 788 spread is equivalent to minimize the time spread. Therefore, solving  $\partial\gamma/\partial\gamma_0 = 0$  leads to  
 789  $\gamma_0 = \sqrt{2k''_0 z}$ . In terms of pulse duration  $\Delta t_{\min@L}$  that minimizes the spread at a given location  $L$ :

$$\Delta t_{\min@L} = 2\sqrt{2 \log(2) k''_0 L} \quad (40)$$

790 Expressing  $\Delta t_{\min@L} = K\sqrt{L}$  in femtoseconds and millimeters leads to a constant  $K$  of 21.91 and  
 791 11.58 for a wavelength of 400 and 800 nm, respectively. This corroborates the correlation of

792 Fig. 6, and confirms that in the investigated variation ranges, the real part of the water refractive  
 793 index can be approximated by its second-order Taylor expansion in  $\lambda$ , as shown in Fig. 17. More  
 794 generally, we estimate the spatial spread of the pulse from the quadratization of the refractive  
 795 index (Eq. 35) as:

$$\Delta s(\Delta t_0, z) = \frac{c_0}{n_0} \sqrt{\Delta t_0^2 + [8 \log(2) k_0'' z / \Delta t_0]^2} \quad (41)$$

796 whose deviation from Eq. 3 is relatively constant (between 2.83 and 2.90%) for  $\lambda_0 = 400$  nm. For  
 797  $\lambda_0 = 800$  nm, the deviation is much heterogeneous, but not depicted here. For a pulse duration  
 798 above 100 fs, the maximum error is 2.5% whereas it increases to 10% when  $\Delta t$  goes to 20 fs.  
 799 These deviations could be considered as acceptable to use Eq. 41 to model the spread of a light  
 800 pulse in the present conditions.

### 801 **Appendix B: Details of the hybrid model for the real part of water refractive index**

802 The matching of the database of from Harvey *et al.* [27] and Segelstein [28] is achieved by a third  
 803 order spline that matches the zeroth and first derivative of both models:

$$S(\lambda) = -7.724559 \times 10^{19} \lambda^3 + 1.697097 \times 10^{14} \lambda^2 - 6.023895 \times 10^7 \lambda + 7.301508 \quad (42)$$

804 with  $\lambda$  in meter. The model is recalled in Table. 2 We consider that the refractive index of water  
 does not vary for wavelengths larger than 1 cm.

Table 2. Hybrid model for the refractive index of water

$\lambda_0$	100 – 175 nm	175 – 200 nm	200 nm – 2.5 $\mu\text{m}$	2.5 $\mu\text{m}$ – 1 cm
Database	Segelstein [28]	Eq. 42	Harvey <i>et al.</i> [27]	Segelstein [28]

805

### 806 **Appendix C: Validation of polydispersity on simple cases**

807 We choose a simple case made of three different diameters, where each droplet scatters light  
 808 only in forward direction ( $\theta = 0^\circ$ ) with two peaks, one for diffraction and one for refraction.  
 809 Their time and normalized intensity are labeled  $(t_{ij}, I_{ij})$  for the diameter  $d_i$  and  $j^{\text{th}}$  peak. Their  
 810 numeric values are summarized in Table 3. The times of the second peak were slightly modified  
 to ease the visualization. We limited the simulation to two scattering events exactly, thus leading

Table 3. Time (in femtosecond) and normalized intensity of the two peaks for each diameter.

	$d_0$	$d_1$	$d_2$
Diffraction peak	(0, 1)	(0, 1)	(0, 1)
Refraction peak	(100, $6.387 \times 10^{-5}$ )	(110, $5.517 \times 10^{-5}$ )	(115, $4.821 \times 10^{-5}$ )

811

812 to only one discrete convolution for the time signal. To post-process the result we did not  
 813 convolve by the pulse signal in order to separate each peak. Each numerical photon depicts a  
 814 comb signal which is normalized so that its time integral is equal to an elementary amount of  
 815 energy set arbitrarily to one. Since the time step is constant, in our simplified case we have  
 816  $(I_{i_0} + I_{i_1})(I_{i_0} + I_{i_1}) = 1$  for two scattering events. As illustrated in Fig. 18(a), there are four  
 817 peaks, one for pure diffraction, two for one refraction and one for two refractions. Their time is 0,  
 818  $t_{i_0,1}$ ,  $t_{i_1,1}$  and  $t_{i_0,1} + t_{i_1,1}$ , respectively, and their probability is given by the previous equation. The

819 total signal is made of one pure diffraction peak of amplitude unity, a first group of three peaks  
 820 due to one refraction and a second group of six peaks due to two refractions. An example is  
 821 given in Fig. 18 (b) for a uniform distribution. The sum of all peaks is given by:

$$S = 1 + \sum_{(i,j)} p_i p_j (I_{d_i,1} + I_{d_j,1}) + \sum_{(i,j)} (p_i I_{d_i,1}) (p_j I_{d_j,1}) \quad (43)$$

822 where  $p_i$  is the probability to have the diameter  $d_i$ . The peaks amplitude, depending on its group,  
 823 is given in Table 4. First, we investigated the time signal when the three diameters are uniformly  
 824 distributed, hence  $p_i = 1/3$  for all diameters. The time signal is shown in Fig. 18(b) where  
 825 the peaks are due to one refraction are between  $t = 100$  and  $120$  fs and those of two refraction  
 826 are between  $t = 200$  and  $235$  fs. Their amplitude is estimated from Table 4 and match well the  
 simulation as shown in Fig. 18 (c) and (d). The second case is made of three diameters following

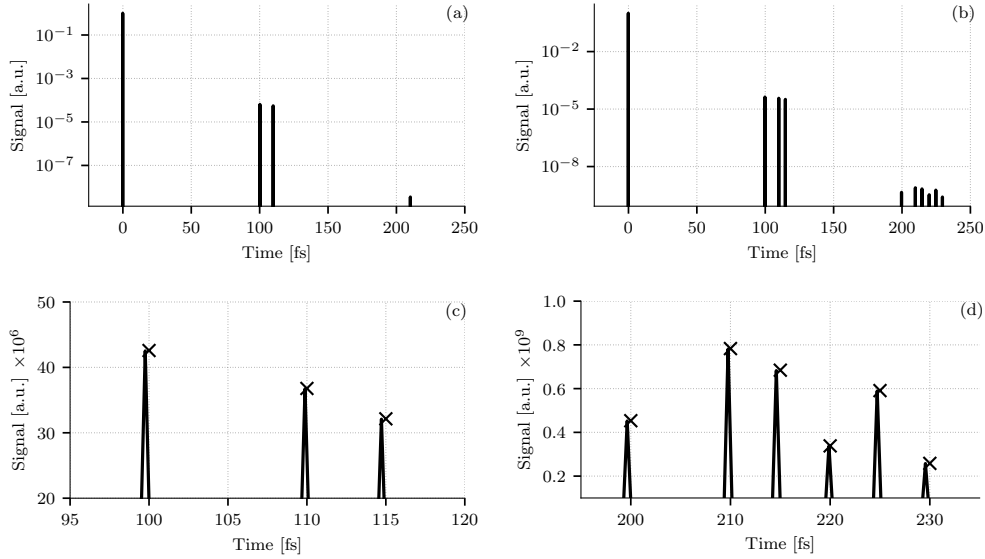


Fig. 18. a) Example of a single photon. b) Signal for a uniform diameter distribution. c) Closeup for one-refraction peaks. d) Closeup for two-refraction peaks.

Table 4. Formulas to calculate times and amplitudes of the peaks due to refraction

	Time	Amplitude	Indices
One diffraction group	$t_i$	$2p_i I_{d_i,1}/S$	$i \in \llbracket 0, 2 \rrbracket$
Two diffraction group (same diam.)	$2t_i$	$p_i^2 I_{d_i,1}^2/S$	$i \in \llbracket 0, 2 \rrbracket$
Two diffraction group (diff. diam.)	$t_i + t_j$	$2 p_i p_j I_{d_i,1} I_{d_j,1}/S$	$(i, j)^2 \in \llbracket 0, 2 \rrbracket^2, i \neq j$

827  
 828 a Gaussian distribution. The two extreme diameters are at  $3\sigma$  while the middle one is on the  
 829 mean. The probabilities are thus  $p_0 = p_2 = 0.0228$  and  $p_1 = 0.9545$ . The amplitudes of the  
 830 peaks are once again calculated with Table 4 and the good agreement is shown in Fig 19. The  
 831 results presented here ensure that the diameter distribution is correctly predicted by our model.

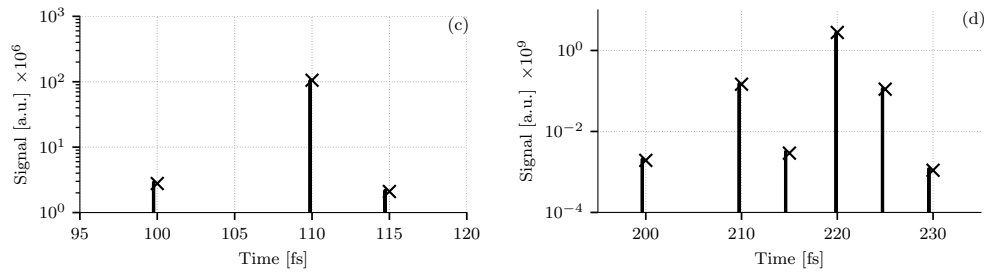


Fig. 19. Left: closeup for one-refraction peaks. Right: closeup for two-refraction peaks.

## References

- 832 1. B. Kunnen, C. Macdonald, A. Doronin, S. Jacques, M. Eccles, and I. Meglinski, "Application of circularly polarized  
833 light for non-invasive diagnosis of cancerous tissues and turbid tissue-like scattering media," *J. Biophotonics* **8**,  
834 317–323 (2015). [eprint: https://onlinelibrary.wiley.com/doi/pdf/10.1002/jbio.201400104](https://onlinelibrary.wiley.com/doi/pdf/10.1002/jbio.201400104).
- 835 2. M. A. Linne, M. Paciaroni, E. Berrocal, and D. Sedarsky, "Ballistic imaging of liquid breakup processes in dense  
836 sprays," *Proc. Combust. Inst.* **32**, 2147–2161 (2009).
- 837 3. A. Ishimaru, "Wave propagation and scattering in random media. Volume 1 - Single scattering and transport theory,"  
838 Wave propagation scattering random media. Vol. 1, by Ishimaru, A.. New York (NY, USA): Acad. Press. 267 pp. Res.  
839 supported by U.S. Air Force, NSF, NIH, 1978 (1978).
- 840 4. M. Linne, "Imaging in the optically dense regions of a spray: A review of developing techniques," *Prog. Energy*  
841 *Combust. Sci.* **39**, 403–440 (2013).
- 842 5. S. Mujumdar and H. Ramachandran, "Imaging through turbid media using polarization modulation: dependence on  
843 scattering anisotropy," *Opt. Commun.* **241**, 1–9 (2004).
- 844 6. E. Berrocal, S.-G. Pettersson, and E. Kristensson, "High-contrast imaging through scattering media using structured  
845 illumination and Fourier filtering," *Opt. Lett.* **41**, 5612–5615 (2016). Publisher: Optical Society of America.
- 846 7. P. A. Galland, X. Liang, L. Wang, P. P. Ho, R. R. Alfano, K. Breisacher, and L. Liou, "Time-resolved optical imaging  
847 of jet sprays and droplets in highly scattering medium," in *Proceedings of the ASME Heat Transfer and Fluids*  
848 *Engineering Divisions*, (1995). Number: CONF-951135- Publisher: American Society of Mechanical Engineers,  
849 New York, NY (United States).
- 850 8. C. Calba, C. Rozé, T. Girasole, and L. Méès, "Monte Carlo simulation of the interaction between an ultra-short pulse  
851 and a strongly scattering medium: The case of large particles," *Opt. Commun.* **265**, 373–382 (2006).
- 852 9. C. Calba, L. Méès, C. Rozé, and T. Girasole, "Ultrashort pulse propagation through a strongly scattering medium:  
853 simulation and experiments," *JOSA A* **25**, 1541–1550 (2008).
- 854 10. G. Chaussonnet and P. M. Bardet, "Scattering of an ultrashort laser pulse by a spherical air bubble," *Opt. Express* **28**,  
855 27358–27371 (2020). Publisher: Optical Society of America.
- 856 11. M. I. Mishchenko, "Vector radiative transfer equation for arbitrarily shaped and arbitrarily oriented particles: a  
857 microphysical derivation from statistical electromagnetics," *Appl. Opt.* **41**, 7114–7134 (2002). Publisher: Optical  
858 Society of America.
- 859 12. M. I. Mishchenko, "Microphysical approach to polarized radiative transfer: extension to the case of an external  
860 observation point," *Appl. Opt.* **42**, 4963–4967 (2003). Publisher: Optical Society of America.
- 861 13. C. Rozé, T. Girasole, L. Méès, G. Gréhan, L. Hespel, and A. Delfour, "Interaction between ultra short pulses and  
862 a dense scattering medium by Monte Carlo simulation: consideration of particle size effect," *Opt. Commun.* **220**,  
863 237–245 (2003).
- 864 14. G. Gouesbet and G. Gréhan, "Generic Formulation of a Generalized Lorenz-Mie Theory for a Particle Illuminated by  
865 Laser Pulses," *Part. & Part. Syst. Charact.* **17**, 213–224 (2000).
- 866 15. L. Mees, G. Gréhan, and G. Gouesbet, "Time-resolved scattering diagrams for a sphere illuminated by plane wave  
867 and focused short pulses," *Opt. Commun.* **194**, 59–65 (2001).
- 868 16. G. Mie, "Beiträge zur Optik trüber Medien, speziell kolloidaler Metallösungen," *Annalen der Physik* **330**, 377–445  
869 (1908). [eprint: https://onlinelibrary.wiley.com/doi/pdf/10.1002/andp.19083300302](https://onlinelibrary.wiley.com/doi/pdf/10.1002/andp.19083300302).
- 870 17. M. P. L. Sentis, F. R. A. Onofri, L. Méès, and S. Radev, "Scattering of light by large bubbles: Coupling of geometrical  
871 and physical optics approximations," *J. Quant. Spectrosc. Radiat. Transf.* **170**, 8–18 (2016).
- 872 18. C. R. Pollock, "Chapter 4 Ultrafast optical pulses," in *Progress in Optics*, vol. 51 E. Wolf, ed. (Elsevier, 2008), pp.  
873 211–249.
- 874 19. E. Berrocal, D. L. Sedarsky, M. E. Paciaroni, I. V. Meglinski, and M. A. Linne, "Laser light scattering in turbid media  
875 Part I: Experimental and simulated results for the spatial intensity distribution," *Opt. Express* **15**, 10649–10665  
876 (2007). Publisher: Optical Society of America.
- 877

- 878 20. C. Calba, "Interaction entre une impulsion lumineuse ultra-brève et un nuage dense de particules : simulations  
879 numériques et expériences," These de doctorat, Rouen (2008).
- 880 21. P. Jenny, S. Mourad, T. Stamm, M. Vöge, and K. Simon, "Computing light statistics in heterogeneous media based  
881 on a mass weighted probability density function method," *JOSA A* **24**, 2206–2219 (2007). Publisher: Optical Society  
882 of America.
- 883 22. M. Sormaz, T. Stamm, S. Mourad, and P. Jenny, "Stochastic modeling of light scattering with fluorescence using a  
884 Monte Carlo-based multiscale approach," *JOSA A* **26**, 1403–1413 (2009). Publisher: Optical Society of America.
- 885 23. M. Šormaz, T. Stamm, and P. Jenny, "Stochastic modeling of polarized light scattering using a Monte Carlo based  
886 stencil method," *JOSA A* **27**, 1100–1110 (2010). Publisher: Optical Society of America.
- 887 24. M. Šormaz, T. Stamm, and P. Jenny, "Influence of linear birefringence in the computation of scattering phase  
888 functions," *J. Biomed. Opt.* **15**, 055010 (2010). Publisher: International Society for Optics and Photonics.
- 889 25. M. Šormaz, M. Reufer, A. C. Völker, and K. Simon, "Breakdown of the continuum limit approximation to the discrete  
890 scattering events and its influence on the electric field autocorrelation functions of transmitted light," *Phys. Rev. A*  
891 **90**, 053802 (2014). Publisher: American Physical Society.
- 892 26. M. Sormaz, S. Mourad, T. Stamm, and P. Jenny, "Predicting Spectral Halftone Measurements for Different Instruments  
893 Using a New Multi-Scale Approach," *Conf. on Colour Graph. Imaging, Vis.* **2008**, 25–30 (2008).
- 894 27. A. H. Harvey, J. S. Gallagher, and J. M. H. L. Sengers, "Revised Formulation for the Refractive Index of Water  
895 and Steam as a Function of Wavelength, Temperature and Density," *J. Phys. Chem. Ref. Data* **IWPS2019**, 761–774  
896 (1998). Publisher: American Institute of Physics.
- 897 28. D. J. Segelstein, "The complex refractive index of water," Thesis, University of Missouri–Kansas City (1981).  
898 Accepted: 2011-09-06T20:38:49Z.
- 899 29. R. W. Austin and G. Halikas, "The index of refraction of seawater," Technical SIO Ref. No. 76-1, Defense Advanced  
900 Research Projects Agency (1976).
- 901 30. P. Schiebener, J. Straub, J. M. H. Levelt Sengers, and J. S. Gallagher, "Refractive index of water and steam as function  
902 of wavelength, temperature and density," *J. Phys. Chem. Ref. Data* **19**, 677–717 (1990). Publisher: American Institute  
903 of Physics.
- 904 31. M. L. Mesenbrink, "Complex Indices of Refraction for Water and Ice from Visible to Long Wavelengths," Ph.D.  
905 thesis, Air Force Inst. of Tech., Wright-Patterson AFB (1996).
- 906 32. S. Orfanidis, *Electromagnetic Waves and Antennas* (2016).